



# Contact and Bending Durability Calculation for Spiral-Bevel Gears

*Sandeep Vijayakar*  
*Advanced Numerical Solutions, Hilliard, Ohio*

## NASA STI Program . . . in Profile

Since its founding, NASA has been dedicated to the advancement of aeronautics and space science. The NASA Scientific and Technical Information (STI) Program plays a key part in helping NASA maintain this important role.

The NASA STI Program operates under the auspices of the Agency Chief Information Officer. It collects, organizes, provides for archiving, and disseminates NASA's STI. The NASA STI Program provides access to the NASA Technical Report Server—Registered (NTRS Reg) and NASA Technical Report Server—Public (NTRS) thus providing one of the largest collections of aeronautical and space science STI in the world. Results are published in both non-NASA channels and by NASA in the NASA STI Report Series, which includes the following report types:

- **TECHNICAL PUBLICATION.** Reports of completed research or a major significant phase of research that present the results of NASA programs and include extensive data or theoretical analysis. Includes compilations of significant scientific and technical data and information deemed to be of continuing reference value. NASA counter-part of peer-reviewed formal professional papers, but has less stringent limitations on manuscript length and extent of graphic presentations.
- **TECHNICAL MEMORANDUM.** Scientific and technical findings that are preliminary or of specialized interest, e.g., "quick-release" reports, working papers, and bibliographies that contain minimal annotation. Does not contain extensive analysis.
- **CONTRACTOR REPORT.** Scientific and technical findings by NASA-sponsored contractors and grantees.
- **CONFERENCE PUBLICATION.** Collected papers from scientific and technical conferences, symposia, seminars, or other meetings sponsored or co-sponsored by NASA.
- **SPECIAL PUBLICATION.** Scientific, technical, or historical information from NASA programs, projects, and missions, often concerned with subjects having substantial public interest.
- **TECHNICAL TRANSLATION.** English-language translations of foreign scientific and technical material pertinent to NASA's mission.

For more information about the NASA STI program, see the following:

- Access the NASA STI program home page at <http://www.sti.nasa.gov>
- E-mail your question to [help@sti.nasa.gov](mailto:help@sti.nasa.gov)
- Fax your question to the NASA STI Information Desk at 757-864-6500
- Telephone the NASA STI Information Desk at 757-864-9658
- Write to:  
NASA STI Program  
Mail Stop 148  
NASA Langley Research Center  
Hampton, VA 23681-2199



# Contact and Bending Durability Calculation for Spiral-Bevel Gears

*Sandeep Vijayakar*  
*Advanced Numerical Solutions, Hilliard, Ohio*

Prepared under Contract NNC15QA19P

National Aeronautics and  
Space Administration

Glenn Research Center  
Cleveland, Ohio 44135

Trade names and trademarks are used in this report for identification only. Their usage does not constitute an official endorsement, either expressed or implied, by the National Aeronautics and Space Administration.

*Level of Review:* This material has been technically reviewed by NASA technical management OR expert reviewer(s).

Available from

NASA STI Program  
Mail Stop 148  
NASA Langley Research Center  
Hampton, VA 23681-2199

National Technical Information Service  
5285 Port Royal Road  
Springfield, VA 22161  
703-605-6000

This report is available in electronic form at <http://www.sti.nasa.gov/> and <http://ntrs.nasa.gov/>

# Contact and Bending Durability Calculation for Spiral-Bevel Gears

Sandeep Vijayakar  
Advanced Numerical Solutions  
Hilliard, Ohio 43026

## Abstract

Extension of capabilities of ANSOL's software tool Transmission3D (Advanced Numerical Solutions LLC) to predict contact and bending fatigue damage and life of spiral bevel gears. Modeling and comparison of simulation results to experiments conducted on a Spiral Bevel Gear Fatigue Rig at the NASA Glenn Research Center

## 1.0 Objectives

The objective of this project is to extend the capabilities of the gear contact analysis solver Calyx, and associated packages Transmission3D, HypoidFaceMilled, HypoidFaceHobbed.

A calculation process for the surface durability was implemented using the Dowson-Higginson correlation for fluid film thickness. Comparisons to failure data from NASA's Spiral Bevel Gear Fatigue rig were carried out.

A bending fatigue calculation has been implemented that allows the use of the stress-life calculation at each individual fillet point. The gears in the NASA test rig did not exhibit any bending fatigue failure, so the bending fatigue calculations are presented in this report by using significantly lowered strength numbers.

## 2.0 Model Setup

A model of the spiral bevel gear set used in NASA's test rig was first set up. The machine settings and cutter geometry for the gear and pinion were provided by NASA in the form of a .SPA file. The built-in face-milling mesh generator in the HypoidFaceMilled package was used to create the finite element meshes for the pinion and gear.

## 2.1 Contact Pattern Study

The pinion and gear deflect relative to each other under load, causing the contact pattern to shift. The relative deflection of the pinion relative to the gear is represented by three linear deflection numbers  $E$ ,  $P$ , and  $G$ , and one rotation number  $\alpha$ . Their

definitions for a bevel gear pair with a right handed gear are shown in Figure 1.  $E$  represents a change in shaft offset,  $P$  represents the pinion moving away from contact along its axis, and  $G$  represents the gear moving away from contact along its axis.  $\alpha$  represents an increase in shaft angle.

In order to estimate these deflections, the software package Transmission3D was used, and the model shown in Figure 2 was built. This boundary condition in this model is moved away from the gear teeth by including finite element meshes for part of the shaft and the rims. This allows the torsional and hoop type deformation effects to be incorporated, in addition to the usual tooth bending effects. Furthermore, the gear and pinion were supported by a stiffness matrix representation of the support structure. A diagonal stiffness matrix was used.

At any specific torque level, the model can be used to calculate the deformations and stresses, as shown in Figure 3.

The Transmission3D model was run at 2535, 4000, and 6000 in-lb of gear torque, while adjusting the diagonal terms of the support structure stiffness matrix, until the predicted contact patterns matched well with the contact patterns reported by NASA at the same three torque levels. The comparison is shown for the three torque levels in Figure 4, Figure 5, and Figure 6.

## 2.2 Deflections

Once we were satisfied with the contact patterns position, we sampled the deflections at FE nodes in the Transmission3D model below the contacting teeth, as shown in Figure 7. Only the nodes in the red regions were sampled.

Next, a least-squares linear regression was used to determine the combination of the 12 rigid body motion components (six for the pinion and six for the gear) that would best fit these sampled deflections. Finally, the relative rigid body motion between the two bodies was calculated and transformed to the deflection numbers  $E$ ,  $P$ , and  $G$ , and  $\alpha$ .

Deflections at an additional load level of 8000 in-lb gear torque were obtained by linear extrapolation of the deflections at 6000 in-lb gear torque. The deflection results are shown in Table 1.

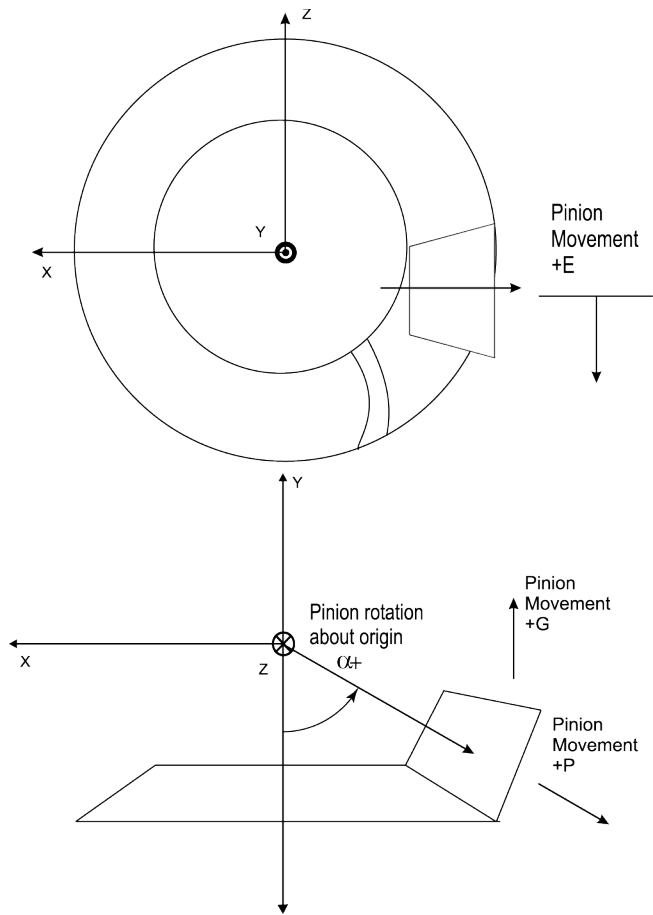


Figure 1.—Definitions and sign convention for deflections in a spiral bevel gear pair with a right handed gear

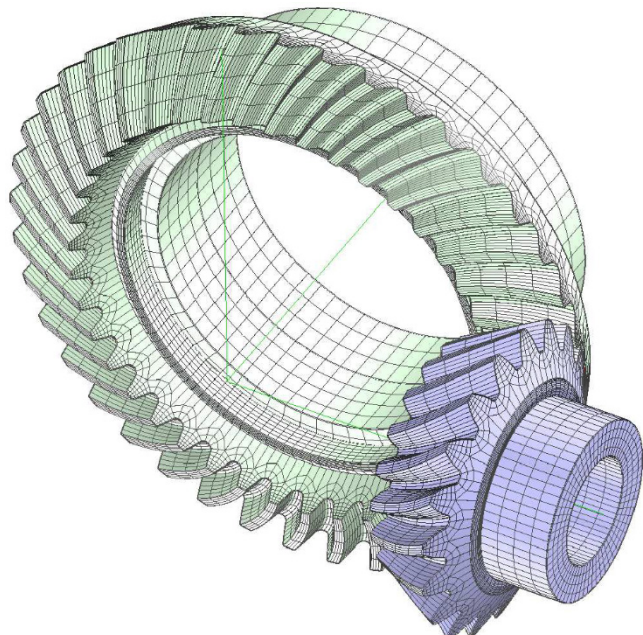


Figure 2.—Finite element mesh in the Transmission3D model.

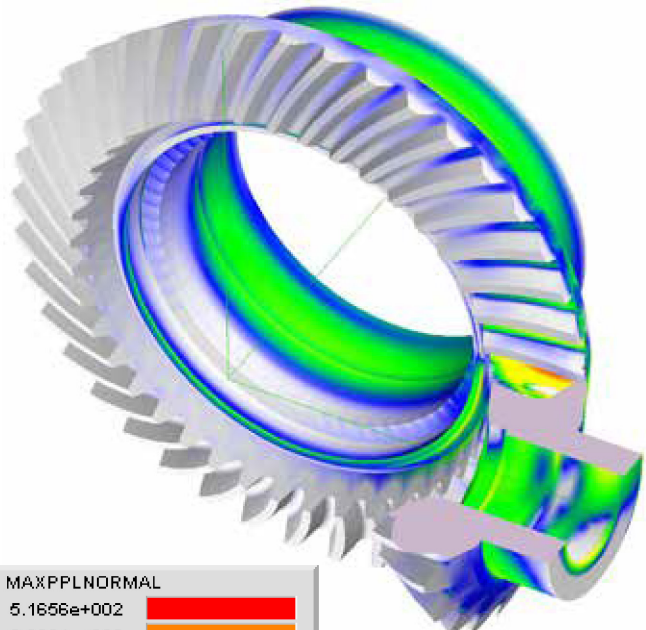


Figure 3.—Distribution of the maximum principal normal stress in the Transmission3D Finite Element model, in MPa at 6000 in-lb of gear torque.

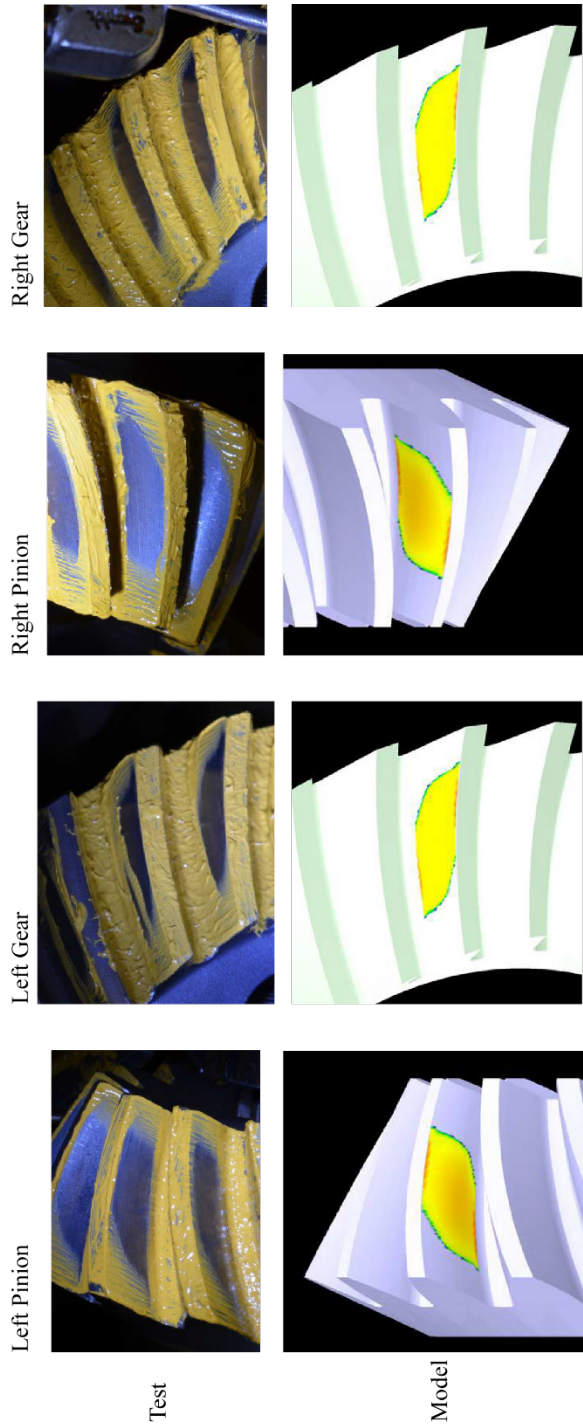


Figure 4.—Contact Patterns at 2535 in-lb of gear torque.

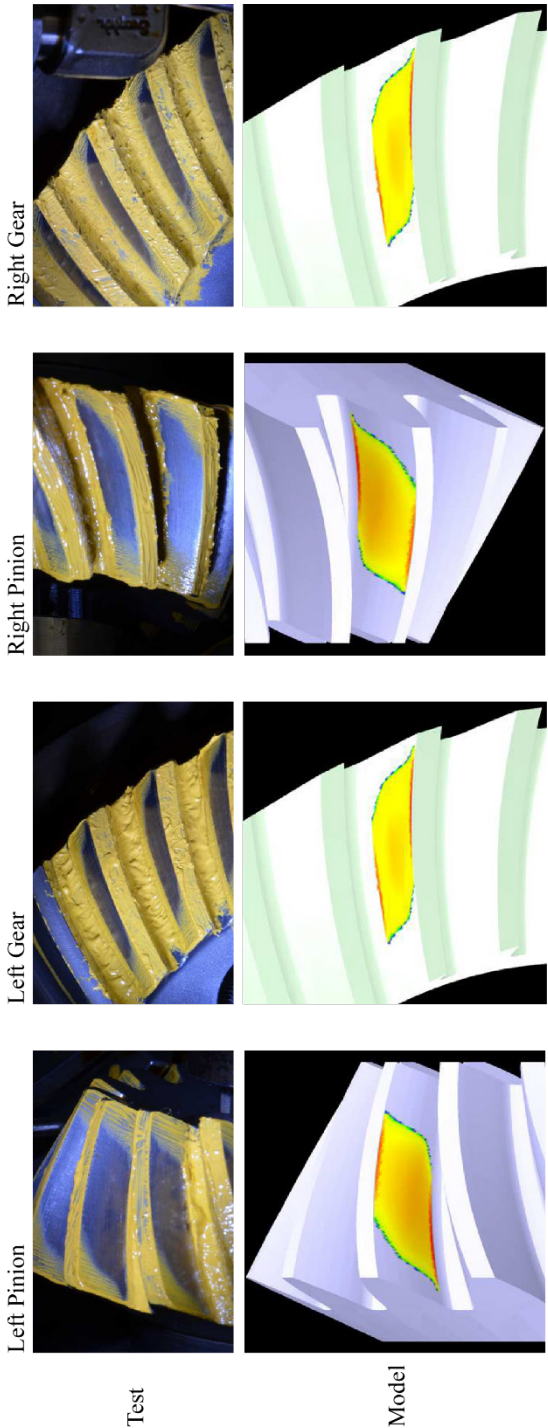


Figure 5.—Contact Patterns at 4000 in-lb of gear torque.

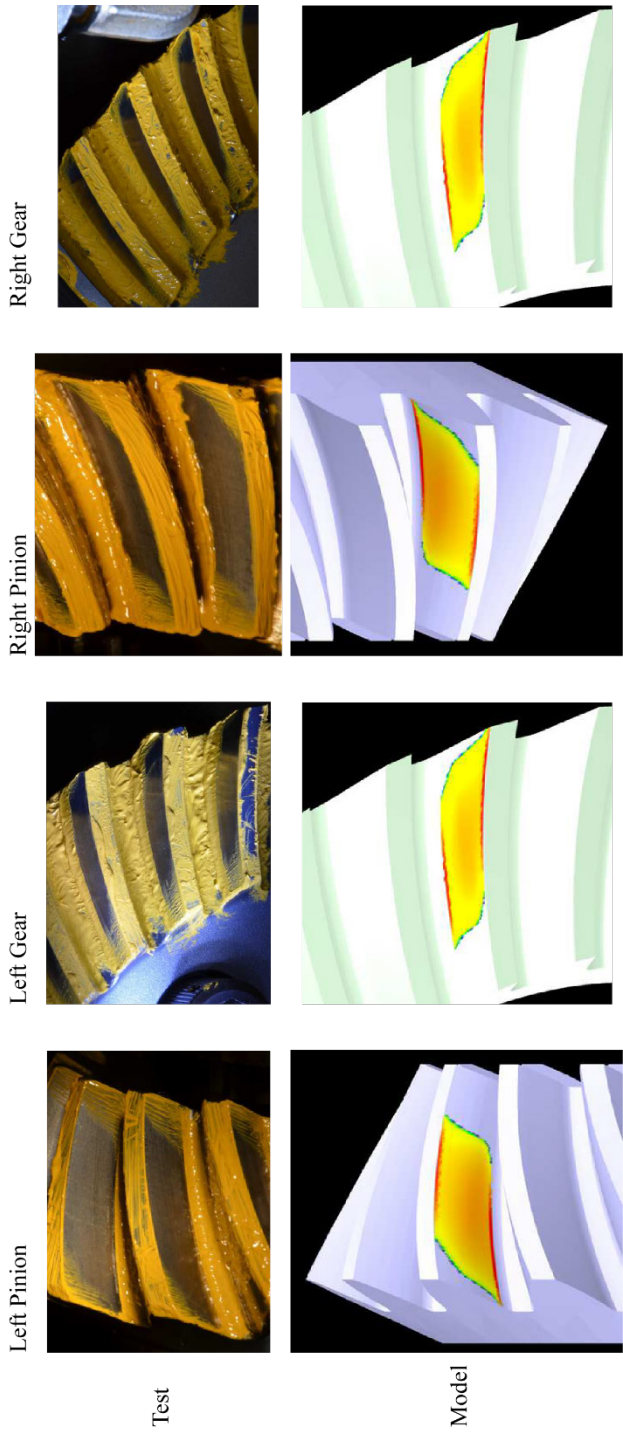


Figure 6.—Contact Patterns at 6000 in-lb of gear torque.

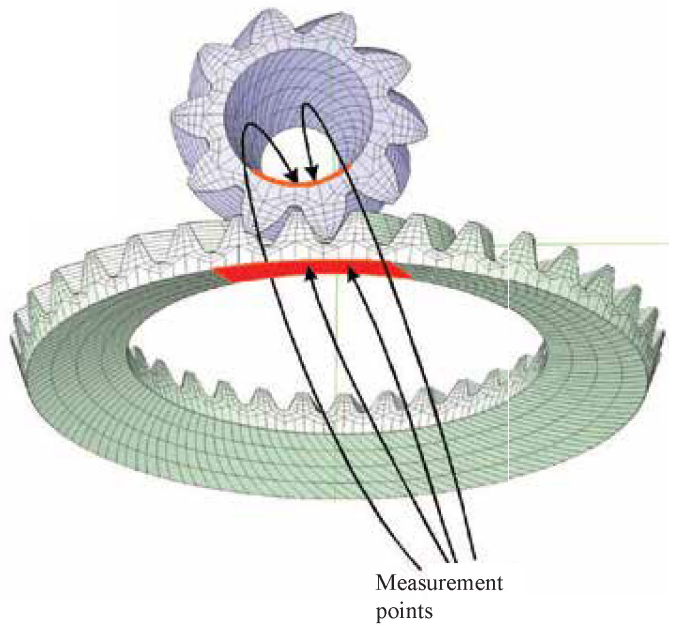


Figure 7.—Sampling the Transmission3D model to calculate deflections  $E$ ,  $P$ ,  $G$ ,  $\alpha$  that can be used as boundary conditions for a simpler HypoidFaceMilled model. The parts of the model colored in red are where FE nodes were sampled.

TABLE 1.—SYSTEM DEFLECTIONS ESTIMATED FROM CONTACT PATTERN STUDY

Gear torque, in-lb	$E$ , mm	$P$ , mm	$G$ , mm	$\alpha$ , °
2535.0	-0.1161	0.0577	-0.00852	0.00490
4000.0	-0.1797	0.0903	-0.01527	0.00920
6000.0	-0.2639	0.1345	-0.02600	0.01621
8000.0	-0.3518	0.1793	-0.03467	0.02161

These deflections were then imposed as boundary conditions on the simpler HypoidFaceMilled model that was then used in the surface durability and bending durability calculations. HypoidFaceMilled models run much faster than the larger Transmission3D model. However, if computer time were no object, the surface durability calculations could have been conducted solely with the larger Transmission3D model.

### 3.0 Post-Processed Contact Data

Running the HypoidFaceMilled model yields detailed information about the state of contact at each instant of time. Snapshots of instantaneous contact pressure, load intensity and sliding and rolling velocities are shown in Figure 8 to Figure 11.

The instantaneous data is then interpolated using the PATTERN post-processing command. All the necessary inputs to film thickness and durability calculation are output in tab-delimited form. We loaded this data into a Microsoft Excel spreadsheet (Microsoft Corporation), and programmed the film thickness and Lundberg-Palmgren calculations as macros in Excel Visual Basic for Applications. We are providing the source code for these macros to NASA.

Two-dimensional contour plots, generated by Excel, of this PATTERN command output data are shown in Figure 12 to Figure 20.

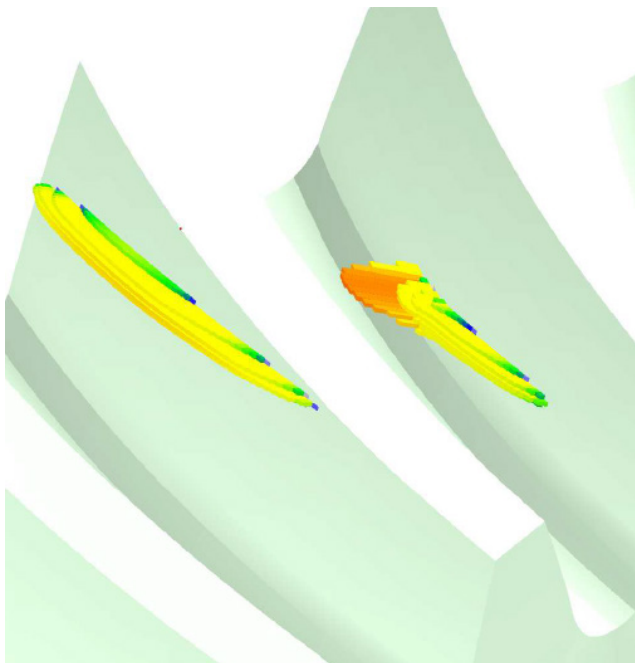


Figure 8.—Instantaneous contact pressure distribution drawn on the gear tooth, at 8000 in-lb of gear torque. Note the high contact pressure at the edges. Also note that the contact zone is not purely elliptical, as would be predicted by Hertz theory.

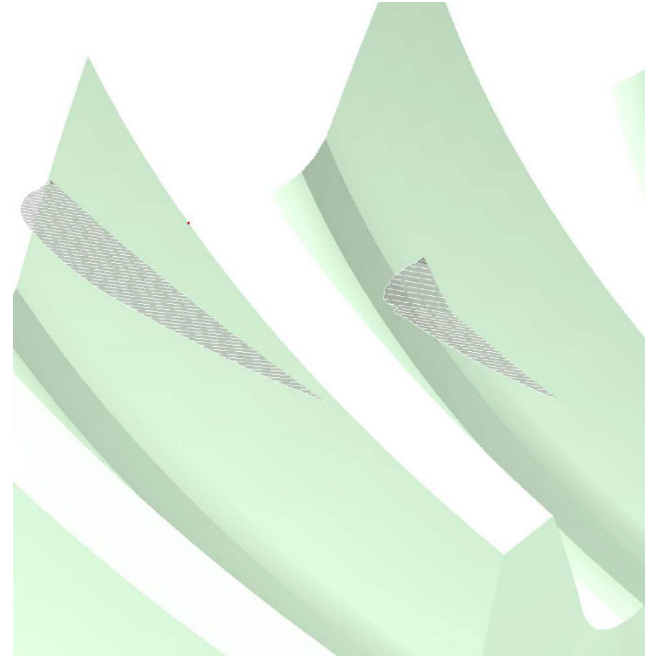


Figure 9.—Instantaneous load intensity drawn on the gear tooth, at 8000 in-lb of gear torque. The load intensity is the load per unit length along the 'line of contact'. It is obtained by summing up the contact pressures across the width of the contact zone.

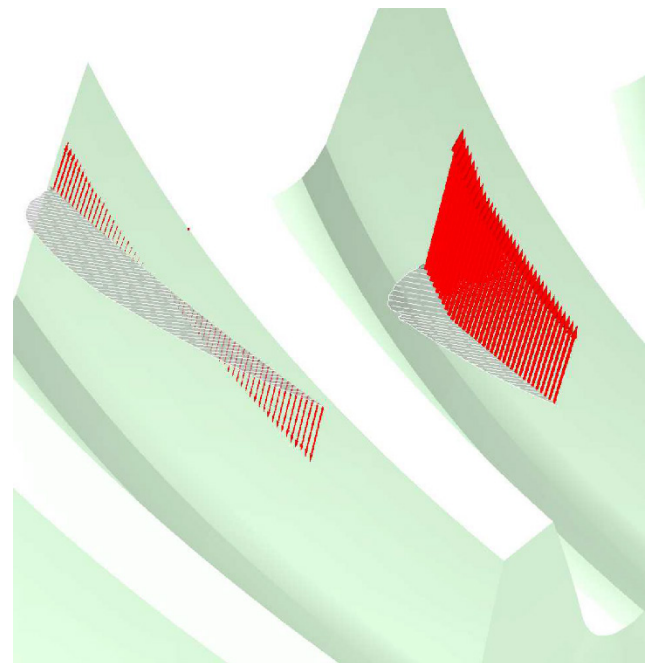


Figure 10.—Instantaneous sliding velocities observed on the gear tooth, at 8000 in-lb of gear torque. The length of the red arrows indicates the magnitude of sliding velocity. The sliding velocity is the relative velocity between the pinion and gear surfaces, so it will be equal and opposite when observed on the pinion. Note the change in direction of the sliding velocity vector at the pitch cone. Also note that the direction of sliding is mostly in the transverse plane, similar to spur and helical gears. This is because this gear set has no hypoid offset.

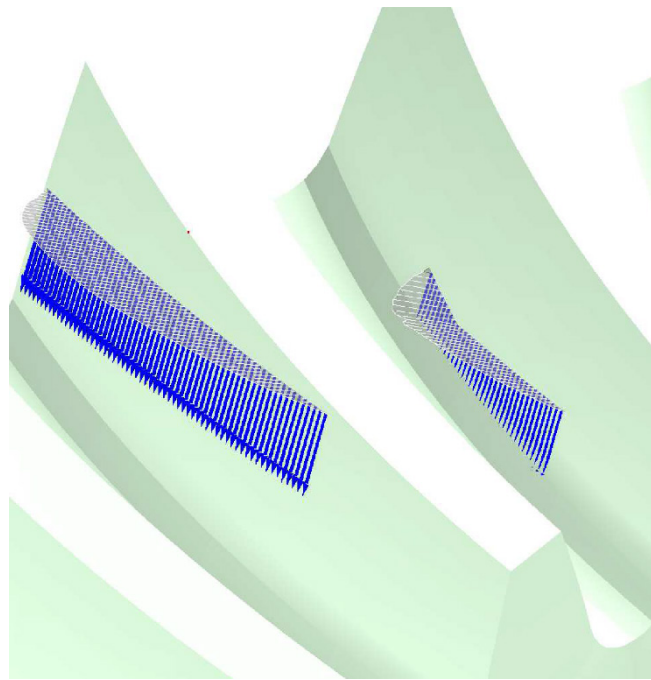


Figure 11.—Instantaneous rolling velocities observed on the gear tooth, at 8000 in-lb of gear torque. The length of the blue arrows indicates the magnitude of rolling velocity. The rolling velocity is defined as the velocity of the contact zone relative to the surface of the tooth. It does not change direction, and always points from the entry of contact to the exit of contact. Only the component perpendicular to the contact ellipse has been shown. The vector difference of the rolling velocities on the pinion and gears equals the sliding velocity.

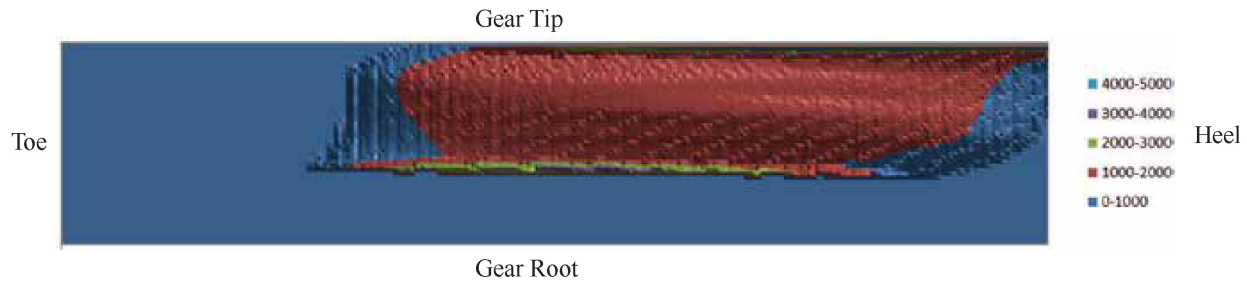


Figure 12.—Contact pressure ( $p$ , MPa) drawn on the gear surface. Gear torque is 8000 in-lb.

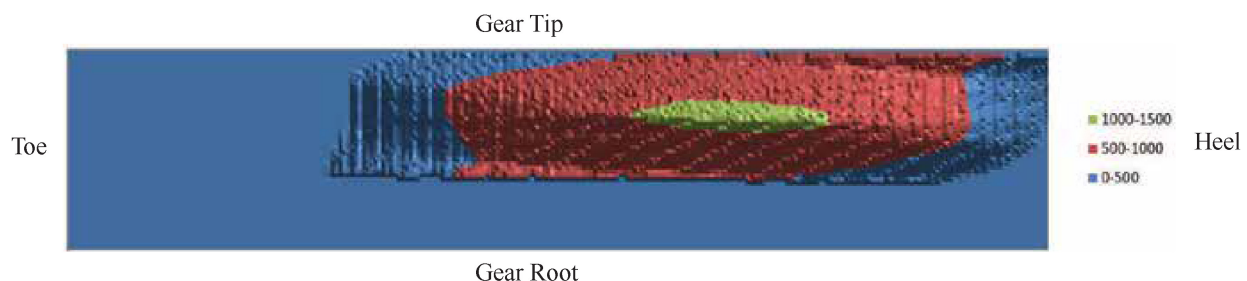


Figure 13.—Contact load intensity ( $L$ , N/mm) drawn on the gear surface. Gear torque is 8000 in-lb.

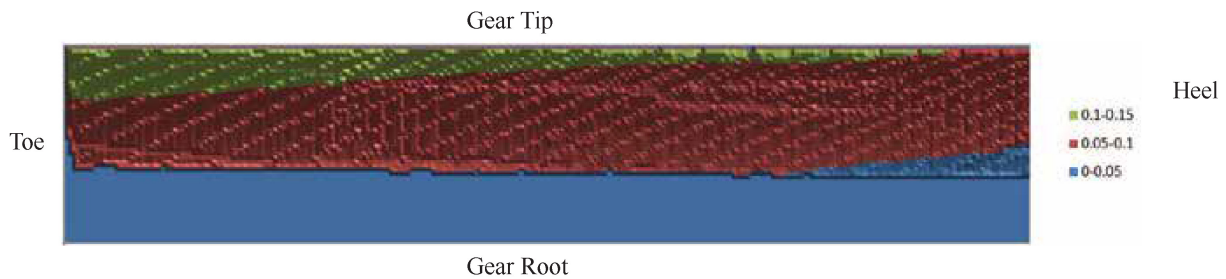


Figure 14.—Relative normal curvature ( $1/\rho_{n,c}$ ,  $\text{mm}^{-1}$ ) drawn on the gear surface. Gear torque is 8000 in-lb.

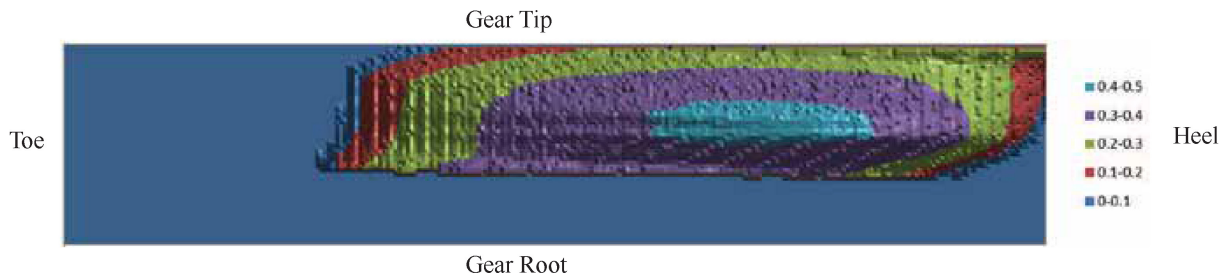


Figure 15.—Hertz semi-width ( $b$ , mm) drawn on the gear surface. Gear torque is 8000 in-lb.

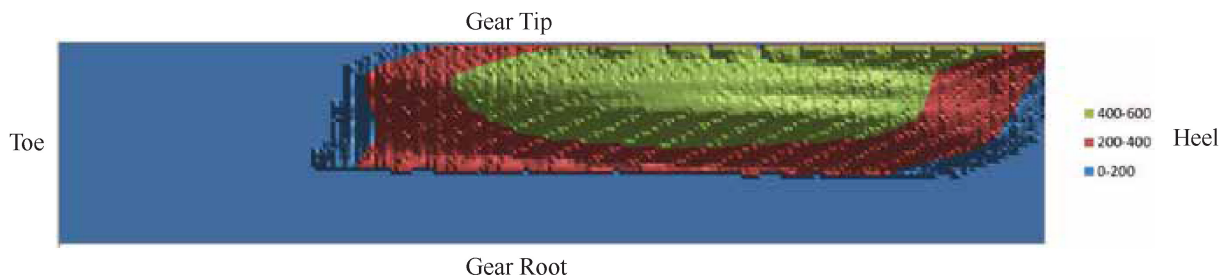


Figure 16.—Max sub-surface max shear ( $\tau_{\max}$ , MPa) drawn on the gear surface. Gear torque is 8000 in-lb.

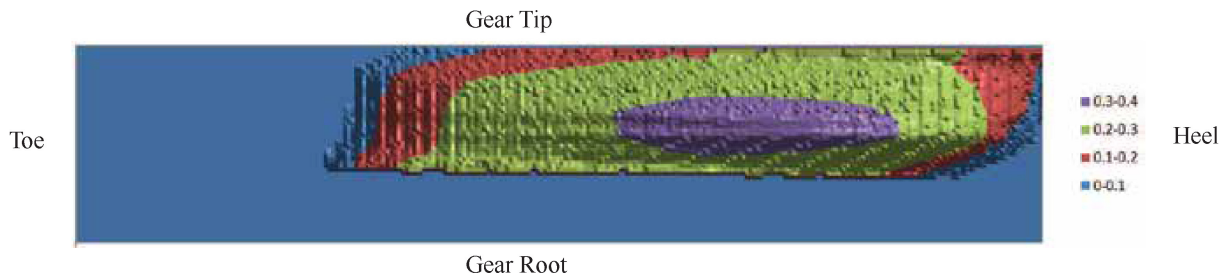


Figure 17.—Depth of max sub-surface max shear ( $z_1$ , mm) drawn on the gear surface. Gear torque is 8000 in-lb.

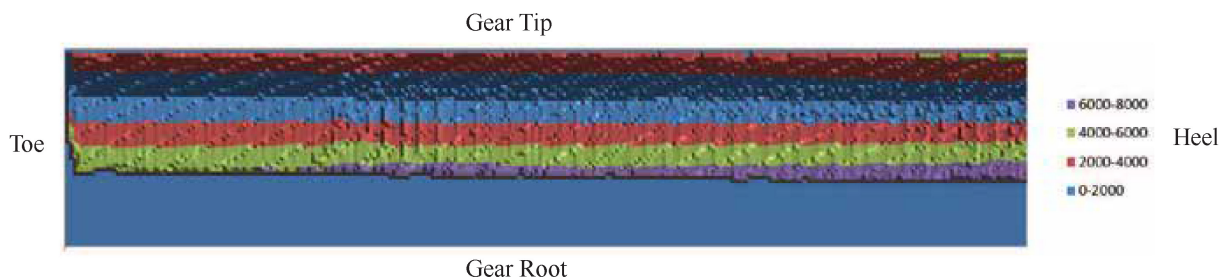


Figure 18.—Magnitude of sliding velocity ( $V_s$ , mm/s) drawn on the gear surface. Gear torque is 8000 in-lb.

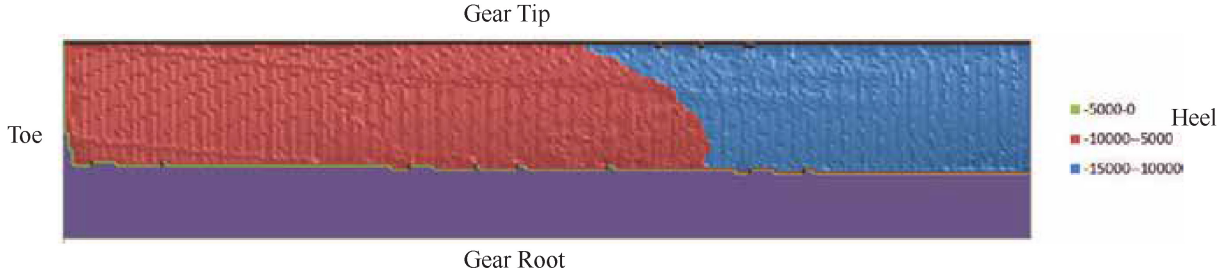


Figure 19.—Magnitude of rolling velocity ( $V_1$ , mm/s) drawn on the gear surface. Gear torque is 8000 in-lb.

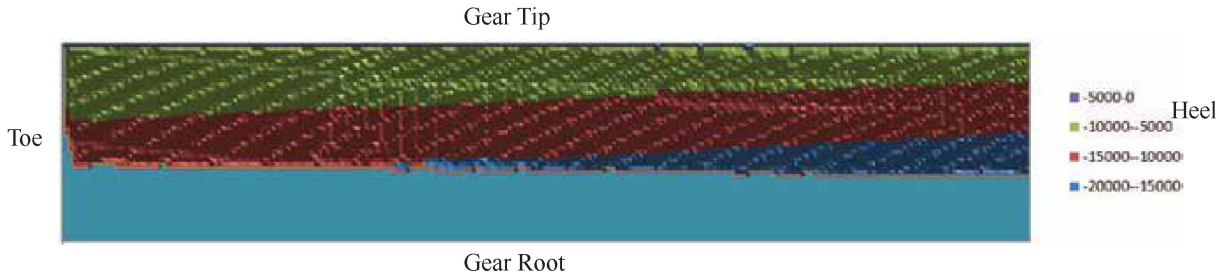


Figure 20.—Magnitude of rolling velocity ( $V_2$ , mm/s) drawn on the gear surface. Gear torque is 8000 in-lb.

TABLE 2.—LUBRICANT PARAMETERS

Pressure-visc. coeff. at 38 °C, $\alpha_{38}$ .....	$1.10 \times 10^{-8} \text{ m}^2/\text{N}$
Kinematic viscosity at 40 °C, $\nu_{40}$ .....	$28.4 \text{ mm}^2/\text{s}$ or $cSt$
Kinematic viscosity at 100 °C, $\nu_{100}$ .....	$5.37 \text{ mm}^2/\text{s}$ or $cSt$
Bulk temperature, $\theta_M$ .....	135 °C
Density at 15 °C, $\rho_{15}$ .....	$990 \text{ kg/m}^3$

TABLE 3.—STEEL PARAMETERS AND SURFACE ROUGHNESS

Specific heat conductivity, $\lambda_{M1}, \lambda_{M2}$ .....	$45 \text{ W/mK}$
Specific heat capacity, $c_{M1}, c_{M2}$ .....	$440 \text{ J/kgK}$
Young's Modulus, $E_1, E_2$ .....	$206,842 \text{ MPa}$
Poisson's Ratio, $\nu_1, \nu_2$ .....	0.3
Density, $\rho_{M1}, \rho_{M2}$ .....	$7800 \text{ kg/m}^3$
Surface roughness, $R_{a1}, R_{a2}$ .....	$0.4064 \mu\text{m}$

## 4.0 Surface Durability Calculation

This section describes the calculation of the central film thickness. The film thickness is used to compute life correction factor (Skurka (Ref. 1)) and is applied to local Lundberg-Palmgren  $L_{10}$  life.

The coefficient of friction and flash temperature calculations are based on the development in the standard ISO/15144-1 (Ref. 2). We have modified the calculations so that involute relations are not used for any of the curvature, rolling or sliding velocity inputs. Numerically calculated values from the PATTERN post-processing, as described in the previous section, were used instead.

The lubricant properties used are shown in Table 2. This corresponds to Lubricant H in Table 4 of Krantz and Kahraman (Ref. 3). Steel properties shown in Table 3 were used for the gear and pinion material.

### 4.1 Local Viscosity and Density

As a first step, the value of kinematic viscosity  $\nu_{\theta M}$  at the specified bulk temperature  $\theta_M$  is obtained from the values of kinematic viscosity at 40 and 100 °C

$$\nu_{\theta M} = 10^{A \cdot \log_{10}(\theta_M + 273) + B} - 0.7$$

where,

$$A = \frac{\log_{10}[\log_{10}(\nu_{40} + 0.7) / \log_{10}(\nu_{100} + 0.7)]}{\log_{10}(313/373)}$$

$$B = \log_{10}[\log_{10}(\nu_{40} + 0.7)] - A \cdot \log_{10} 313$$

$\nu_{40}$  kinematic viscosity at 40 °C,  $\text{mm}^2/\text{s}$

$\nu_{100}$  kinematic viscosity at 100 °C,  $\text{mm}^2/\text{s}$

Similarly the density at  $\rho_{\theta M}$  at the specified bulk temperature  $\theta_M$  is obtained by extrapolating the value of density at 15 °C:

$$\rho_{\theta M} = \rho_{15} \left[ 1 - 0.7 \cdot \frac{(\theta_M + 273) - 289}{\rho_{15}} \right]$$

where  $\rho_{15}$  is the density of lubricant at 15 °C, in kg/m<sup>3</sup>.

Then the dynamic viscosity at the bulk temperature  $\eta_{\theta M}$  is calculated using kinematic viscosity and density at the bulk temperature:

$$\eta_{\theta M} = 10^{-6} \cdot v_{\theta M} \cdot \rho_{\theta M}$$

where,

$\eta_{\theta M}$  dynamic viscosity at bulk temperature, Ns/m<sup>2</sup>  
 $v_{\theta M}$  kinematic viscosity at bulk temperature, mm<sup>2</sup>/s  
 $\rho_{\theta M}$  density of lubricant at bulk temperature, kg/m<sup>3</sup>

#### 4.1.1 Coefficient of Friction

The local coefficient of friction  $\mu$  varies with local load, curvature and velocity conditions. So it is different at every location on the surface. It is computed using the following equation based on standard ISO/15144-1 (Ref. 2). The factors compensating for the nominal load and dynamic factor have been ignored, and set to 1.0 in the equation.

$$\mu = 0.045 \left( \frac{K_A \cdot K_V \cdot K_{H\alpha} \cdot K_{H\beta} \cdot K_{H\gamma} \cdot L_I}{V_r \cdot \rho_{n,c}} \right)^{0.2} \left( 10^3 \cdot \eta_{\theta M} \right)^{-0.05} X_R X_L$$

where,

$$X_R = 2.2 \left( \frac{R_a}{\rho_{n,c}} \right)^{0.025}$$

$$X_L = 1.0$$

$$K_A, K_V, K_{H\alpha}, K_{H\beta}, K_{H\gamma} = 1.0$$

Note that in the expression for  $X_R$  above,  $R_a$  is in  $\mu\text{m}$ , while  $\rho_{n,c}$  is in mm.

$X_R$  roughness factor  
 $R_a$  effective arithmetic mean roughness in  $\mu\text{m}$   
 $R_a = (R_{a1} + R_{a2})/2$  in  $\mu\text{m}$   
 $L_I$  load intensity, N/mm  
 $V_r$  Sum of rolling velocities ( $V_{r1} + V_{r2}$ ), m/s  
 $\rho_{n,c}$  Normal radius of relative curvature, mm  
 $\theta_M$  bulk temperature, Celsius  
 $\eta_{\theta M}$  dynamic viscosity at bulk temperature, Ns/m<sup>2</sup>  
 $K_A = 1.0$ , application factor  
 $K_V = 1.0$ , dynamic factor  
 $K_{H\alpha} = 1.0$ , transverse load factor  
 $K_{H\beta} = 1.0$ , face load factor

$K_{H\gamma} = 1.0$ , helical load factor

$X_L = 1.0$ , lubrication factor

Figure 21 shows the distribution over the contacting surface of  $\mu$  at 8000 in-lb of gear torque.

#### 4.2 Flash Temperature

The flash temperature  $\theta_f$  is the difference between the contact temperature  $\theta_B$  and the bulk temperature  $\theta_M$ . The equation to calculate the flash temperature  $\theta_f$  in Celsius is

$$\theta_f = \frac{\sqrt{\pi}}{2} \frac{10^6 \cdot \mu \cdot H_s \cdot |V_s|}{B_{M1} \sqrt{V_{r1}} + B_{M2} \sqrt{V_{r2}}} \sqrt{8\kappa \frac{H_s}{1000 E_r}}$$

where

$$B_{M1} = \sqrt{\rho_{M1} \cdot \lambda_{M1} \cdot c_{M1}}$$

$$B_{M2} = \sqrt{\rho_{M2} \cdot \lambda_{M2} \cdot c_{M2}}$$

$$E_r = 2 \left( \frac{1 - v_1^2}{E_1} + \frac{1 - v_2^2}{E_2} \right)^{-1}$$

and

$\theta_f$  flash temperature, Celsius  
 $\mu$  coefficient of friction  
 $B_{M1}, B_{M2}$  thermal coefficient of member 1 and member 2  
 $\lambda_{M1}, \lambda_{M2}$  specific heat conductivity, W/mK of member 1 and member 2, (for steel: 45 W/mK)  
 $c_{M1}, c_{M2}$  specific heat capacity, J/kgK of member 1 and member 2, (for steel: 440 J/kgK)  
 $\rho_{M1}, \rho_{M2}$  density of member 1 and member 2, kg/m<sup>3</sup>  
 $E_1, E_2$  Young's Modulus of member 1 and member 2, N/mm<sup>2</sup>  
 $v_1, v_2$  Poisson's Ratio of member 1 and member 2  
 $E_r$  reduced modulus of elasticity, N/mm<sup>2</sup>  
 $H_s$  contact pressure, N/mm<sup>2</sup>  
 $V_s$  sliding velocity, m/s  
 $V_{r1}, V_{r2}$  rolling velocity of member 1 and member 2, m/s  
 $\kappa$  normal radius of relative curvature, mm

Note that like many empirical relationships, this flash temperature equation is units sensitive because of the inconsistent choice of units for various parameters.

The variation of flash temperature  $\theta_f$  over the gear surface at 8000 in-lb of gear torque is shown in Figure 22.

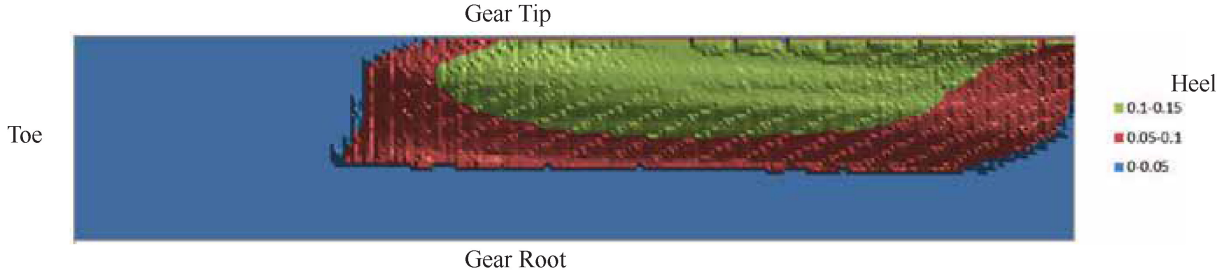


Figure 21.—Coefficient of friction  $\mu$  drawn on the gear surface. Gear torque is 8000 in-lb.

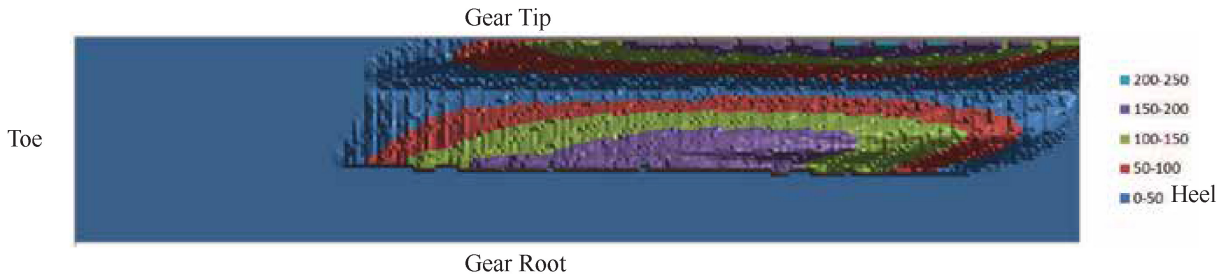


Figure 22.—Flash temperature ( $\theta_f$ , Celsius) drawn on the gear surface. Gear torque is 8000 in-lb.

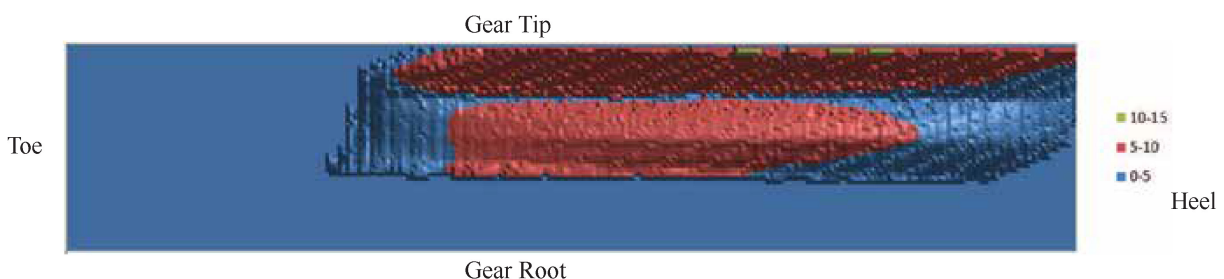


Figure 23.—Reciprocal of specific film thickness ( $1/h_s$ ) drawn on the gear surface. Gear torque is 8000 in-lb.

### 4.3 Film Thickness

Once the flash temperature is calculated, we have everything we need to calculate the specific film thickness. We use a calculation described in the standard ISO/ 15144-1 (Ref. 2), which in turn is based the Dowson-Higginson correlation (Ref. 4). The specific film thickness is the ratio of the local film thickness to surface roughness:

$$h_s = \frac{h_y}{R_a}$$

where the local film thickness is obtained through the correlation:

$$h_y = 1600 \cdot \kappa \cdot G_M^{0.6} \cdot U_Y^{0.7} \cdot W_Y^{-0.13} \cdot S_Y^{0.22}$$

where,

$h_s$  local specific film thickness

$h_y$  local film thickness,  $\mu\text{m}$

$R_a$	effective arithmetic mean roughness value, $\mu\text{m}$
$G_M$	material parameter
$U_Y$	local velocity parameter
$W_Y$	local load parameter
$S_Y$	local sliding parameter

Figure 23 shows the variation of the inverse of the specific film thickness over the gear surface at 8000 in-lb of gear torque.

#### 4.3.1 Material Parameter

$$G_M = 10^6 \cdot \alpha_{\theta M} \cdot E_r$$

$$\alpha_{\theta M} = \alpha_{38} * \left[ 1 + 516 \left( \frac{1}{\theta_M + 273} - \frac{1}{311} \right) \right]$$

where,

$\alpha_{38}$  Pressure viscosity coefficient of the lubricant at 38 C,  $\text{m}^2/\text{N}$

$\theta_M$  Bulk temperature, Celsius

#### 4.3.2 Local Velocity Parameter

$$U_Y = \eta_{\theta M} \frac{V_r}{2000.E_r.\kappa}$$

where,

- $\eta_{\theta M}$  dynamic viscosity at bulk temperature, Ns/m<sup>2</sup>
- $V_r$  sum of rolling velocities ( $V_{r1} + V_{r2}$ ), m/s
- $\nu_{\theta M}$  kinematic viscosity at bulk temperature, mm<sup>2</sup>/s
- $\rho_{\theta M}$  density of lubricant at bulk temperature, kg/m<sup>3</sup>

#### 4.3.3 Local Load Parameter

$$W_Y = \frac{2\pi H_s^2}{E_r^2}$$

where,

- $H_s$  Local contact pressure, N/mm<sup>2</sup>
- $E_r$  Reduced modulus of elasticity, N/mm<sup>2</sup>

#### 4.3.4 Local Sliding Parameter

$$S_G = \frac{\alpha_{\theta B} \cdot \eta_{\theta B}}{\alpha_{\theta M} \cdot \eta_{\theta M}}$$

$$\theta_B = \theta_M + \theta_f$$

where,

- $\alpha_{\theta B}$  pressure viscosity coefficient of the lubricant at contact temperature, m<sup>2</sup>/N
- $\alpha_{\theta M}$  pressure viscosity coefficient of the lubricant at bulk temperature, m<sup>2</sup>/N
- $\eta_{\theta B}$  dynamic viscosity of the lubricant at contact temperature, Ns/m<sup>2</sup>
- $\eta_{\theta M}$  dynamic viscosity of the lubricant at bulk temperature, Ns/m<sup>2</sup>
- $\theta_B$  contact temperature, Celsius

#### 4.4 Skurka Life Correction Factor

Skurka (Ref. 1) describes a lubrication-life factor that can be used to correct the Lundberg-Palmgren  $L_{10}$  life for the effect of lubricant film thickness.

$$L_f = 0.3 + 3.01(1.5 \times 10^{-5})^{c^x}$$

where

$$c = 0.646$$

and

$$x = 10h_{s1} - 8.1$$

The specific film thickness  $h_{s1}$  is based on the RMS roughness:

$$h_{s1} = h_y / \sqrt{R_{q1eff}^2 + R_{q2eff}^2}$$

The surface roughness terms  $R_{q1eff}$  and  $R_{q2eff}$  are effective surface roughness numbers corrected for the Hertzian contact width  $w = 2b$  ( $b$  is the Hertz semi-width), and the digital cutoff metric described by Krantz and Kahraman (Ref. 3):

$$R_{qeff} = R_q \sqrt{w/l_c}$$

$l_c$  is the filter cutoff length used while measuring the surface roughness, and  $R_q = R_a \sqrt{\pi/2}$ . We used  $l_c = 0.8$  mm.

The Skurka life correction factor when plotted as a function of specific film thickness (Figure 24) goes asymptotically close to 0.3 for  $h_{s1} < 0.8$ , and asymptotically close to 3.31 for  $h_{s1} > 2.5$ .

#### 4.5 Lundberg-Palmgren Surface Life Calculation

The Lundberg-Palmgren model has been widely used for the surface durability estimation of bearings (Refs. 5 to 11). Coy Townsend and Zaretsky (Ref. 12) at NASA have used it for the life calculation of spur gears. We follow their development closely.

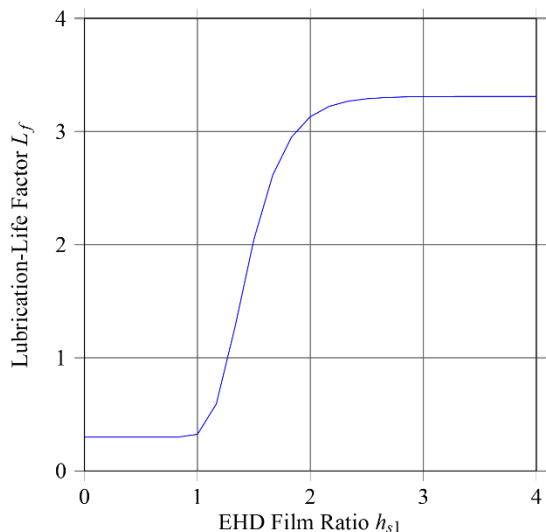


Figure 24.—Skurka (Ref. 1) lubrication-life factor  $L_f$  and  $z_i$  closely tracks the local Hertz semi-width  $b_i$ .

#### 4.5.1 Local Life

The Lundberg-Palmgren failure model is based on the assumption that the probability of survival  $S_i$  of an elemental stressed volume  $\Delta V_i$  as a function of the number of load cycles  $N$  is best approximated by a Weibull probability distribution (Ref. 13) of the type:

$$\ln \frac{1}{S_i} = N^\varepsilon \alpha \frac{\tau_i^c}{z_i^h} \Delta V_i$$

$\varepsilon$  is called the Weibull exponent, and  $\alpha$  is a material constant. Both are meant to be calibrated based on tests.  $c$  is called the stress exponent and  $h$  is called the depth exponent. The constants are usually calibrated while using the value the maximum subsurface ‘orthogonal shear’ stress at the local surface element for  $\tau_i$ , and the depth of this maximum orthogonal shear for  $z_i$ .  $\tau_i$  is closely related to the local contact pressure  $p_i$ ,

$$\tau_i = 0.25 p_i$$

and  $z_i$  closely tracks the local Hertz semi-width  $b_i$ :

$$z_i = 0.49 b_i$$

Both  $p_i$  and  $b_i$  are directly available to us as a result of contact analysis everywhere on the contact surface. Thus the failure probability  $S_i$  can also be calculated anywhere on the contact surface after  $N$  load cycles, as shown in Figure 25.

The orthogonal shear in Equation (1) is not affected by the presence of a residual stress field. But alternative forms of Equation (1) which rely on the maximum shear  $\tau_{\max}(z)$  can be modified to account for a residual stress field. The maximum shear  $\tau_{\max}(z)$  at any depth  $z$  is compensated for the presence of a biaxial state of residual stress  $\sigma_{res}(z)$  to obtain a resultant maximum shear  $\tau_{\max,eff}(z)$  using the relationship:

$$\tau_{\max,eff}(z) = \tau_{\max}(z) + \sigma_{res}(z)/2$$

where  $\sigma_{res}(z)$  is usually negative for a state of compressive residual stress. This relationship assumes that the maximum shear is

$$\tau_{\max}(z) = \max(\tau_{xz}(z), \tau_{yz}(z))$$

$z$  is the depth direction along which the normal component of residual stress is zero, and the normal stress along the  $x$  and  $y$  directions is  $\sigma_{res}(z)$ .

An alternative form for Equation (1) is obtained by substituting 0.9, or 90% as the survival probability  $S_i$ , and the  $L_{10}$  life  $\tilde{L}_{10,i}$  for  $N_i$ :

$$\tilde{L}_{10,i} = \left( \frac{K_1 z_i^h}{\tau_i^c \Delta V_i} \right)^{\frac{1}{\varepsilon}} \quad (2)$$

where

$$K_1 = \frac{\ln \frac{1}{0.9}}{\alpha}$$

The local lubrication-life factor  $L_f$  of Skurka is applied to the local life  $\tilde{L}_{10,i}$  to obtain the corrected local life  $L_{10,i}$

$$L_{10,i} = L_f \tilde{L}_{10,i} \quad (3)$$

Summarizing,

$L_{10,i}$  local L10 (10% failure probability) life in millions of load cycles for the elemental volume

$\tau_i$  Critical shear stress shear stress (N/mm<sup>2</sup>)

$z_i$  Depth of critical shear stress (mm)

$\Delta V_i$  Elemental stressed Volume (mm<sup>3</sup>)

$\varepsilon$  Weibull exponent

$c$  Stress exponent

$h$  Depth exponent

$K_1$  Material constant (N<sup>c</sup>mm<sup>-h-2c+3</sup>)

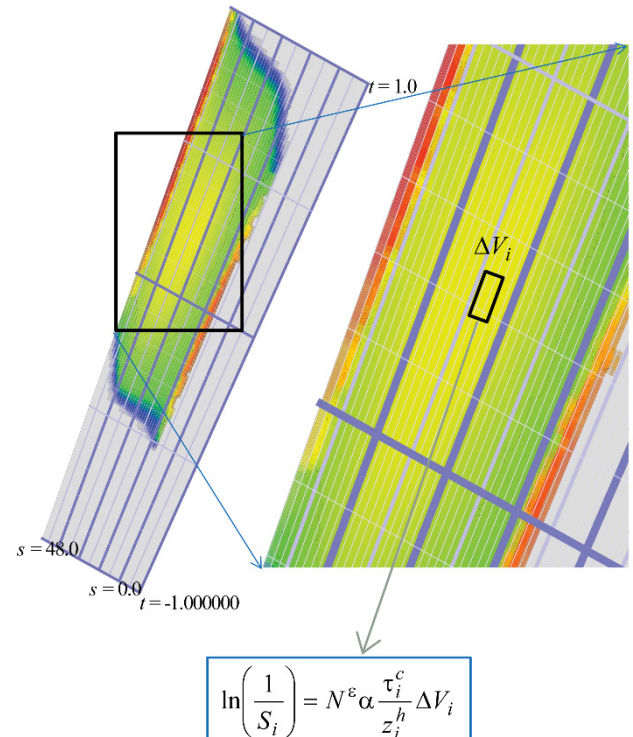


Figure 25.—Life survival probability of a surface element.

The published values for the Weibull, stress, and depth exponents, and also the material constants are shown in Table 4. We have used the values reported by Coy et al. (Ref. 12) in our calculations here.

#### 4.5.2 Component Life

Using the proposition that the all elemental volumes in a component must survive in order for the entire component to survive, the probability of survival  $S$  for a component is the product of the individual elemental probabilities  $S_i$ .

$$S = \prod_i S_i$$

or

$$\ln \frac{1}{S} = \sum_i \ln \frac{1}{S_i}$$

and using Equation (4):

$$\ln \frac{1}{S} = \sum_i N^\varepsilon \alpha \frac{\tau_i^c}{z_i^h} \Delta V_i = N^\varepsilon \sum_i \alpha \frac{\tau_i^c}{z_i^h} \Delta V_i \quad (4)$$

Remarkably, this implies that the *survival probability of a component also follows a Weibull probability distribution function, with the same Weibull exponent*. This is a very important observation, and forms the basis for the Lundberg-Palmgren calculations.

By substituting the 10% failure probability life of the component  $L_{10}$  for  $N$  and 0.9 for the component survival probability  $S$ , and making use of Equation (4), we get a useful expression for the component life  $L_{10}$ :

$$L_{10}^\varepsilon = \sum_i L_{10,i}^\varepsilon \quad (5)$$

The same process can be used to compute the  $L_{10}$  life of a system from that of a component. One merely needs to convert load cycles to a shared measure of duration before applying the summation. In our case, if one converts the life from number of cycles survived to number of minutes survived, then assuming that the Weibull exponent is the same for the pinion and gear,

$$L_{10,sys}^\varepsilon = L_{10,pinion}^\varepsilon + L_{10,gear}^\varepsilon \quad (6)$$

Once the  $L_{10}$  life  $L_{10,sys}$  in minutes is known, the survival probability of the system  $S_{sys}$  at any other time  $t$  (also in minutes) is easily obtained because the system survival probability also follows a Weibull distribution:

$$\ln \frac{1}{S_{sys}} = \ln \left( \frac{1}{0.9} \right) \frac{t^\varepsilon}{L_{10,sys}^\varepsilon} \quad (7)$$

The probability of failure  $S_{failure}$  is simply

$$S_{failure} = 1 - S_{sys} \quad (8)$$

The solid line in the graph of Figure 26 shows the calculated failure probability as a function of time in minutes. Table 6 and Table 5 summarize the observed surface failures in NASA's test rig, and the observations appear as discrete data points in the Weibull plot of Figure 26. The corresponding probability density function for system failure is shown in Figure 27.

The flow chart in Figure 28 summarizes the surface durability calculation process.

TABLE 4.—PARAMETERS USED IN THE LUNDBERG-PALMGREN LIFE MODEL

Parameter	Source		
	Coy et al. (Ref. 12) Spur Gears	Warda et al. (Ref. 11) for bearings	
		Point contact	Line contact
$\varepsilon$	3	10/9	9/8
$c$	31/3	31/3	31/3
$h$	7/3	7/3	7/3
$K_1(N^\varepsilon mm^{-h-2c+3})$	$1.43 \times 10^{35}$	N/A	N/A

TABLE 5.—FAILURE RATE OBSERVED IN TEST CASES

Minutes	% Failed
705	20
1784	40
2120	60
5249	80
6818	100

TABLE 6.—TEST CASES SAMPLED FOR SURFACE FAILURE

[Tests where failure was due to early scuffing have been discarded because no conclusion regarding likelihood of pitting could be drawn from those tests.]

Test case	Observations	Decision
L4545R5050	Pinion pits at 2120 min	Keep
L3030R5050	Pinion pits at 1784 min	Keep
L1515R5050	Pinion pits at 705 min	Keep
L2020R5050	Scuffing at 217 min	Discard
L4040R5050	Scuffing at 370 min	Discard
L3535R5050	Gear pits at 6818 min	Keep
L1818R1616	Pinion pits at 5249 min	Keep
L1212R1919	Scuffing at 307 min	Discard

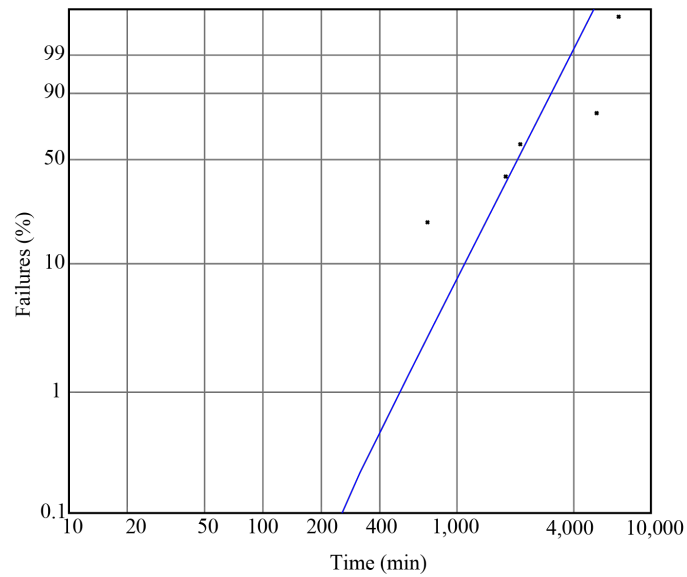


Figure 26.—Weibull plot for system failure.  $L_{10}$  life for the system is 1095 min. Weibull exponent is  $\varepsilon = 3.0$

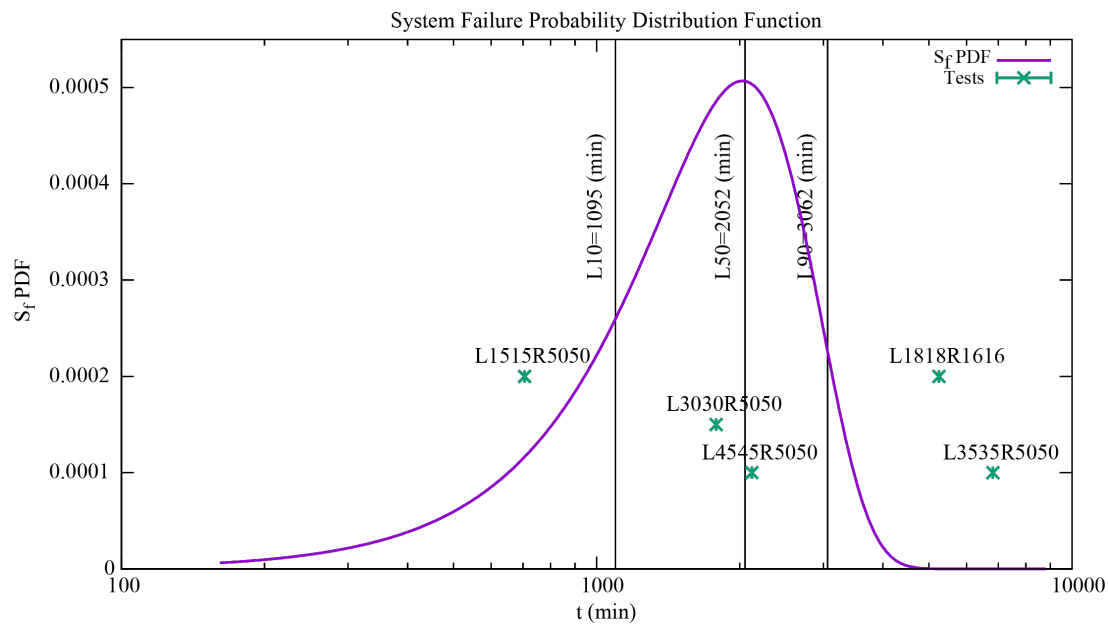


Figure 27.—Weibull failure probability density function for the system. The system failure probability is the probability that either the pinion or gear would have failed.

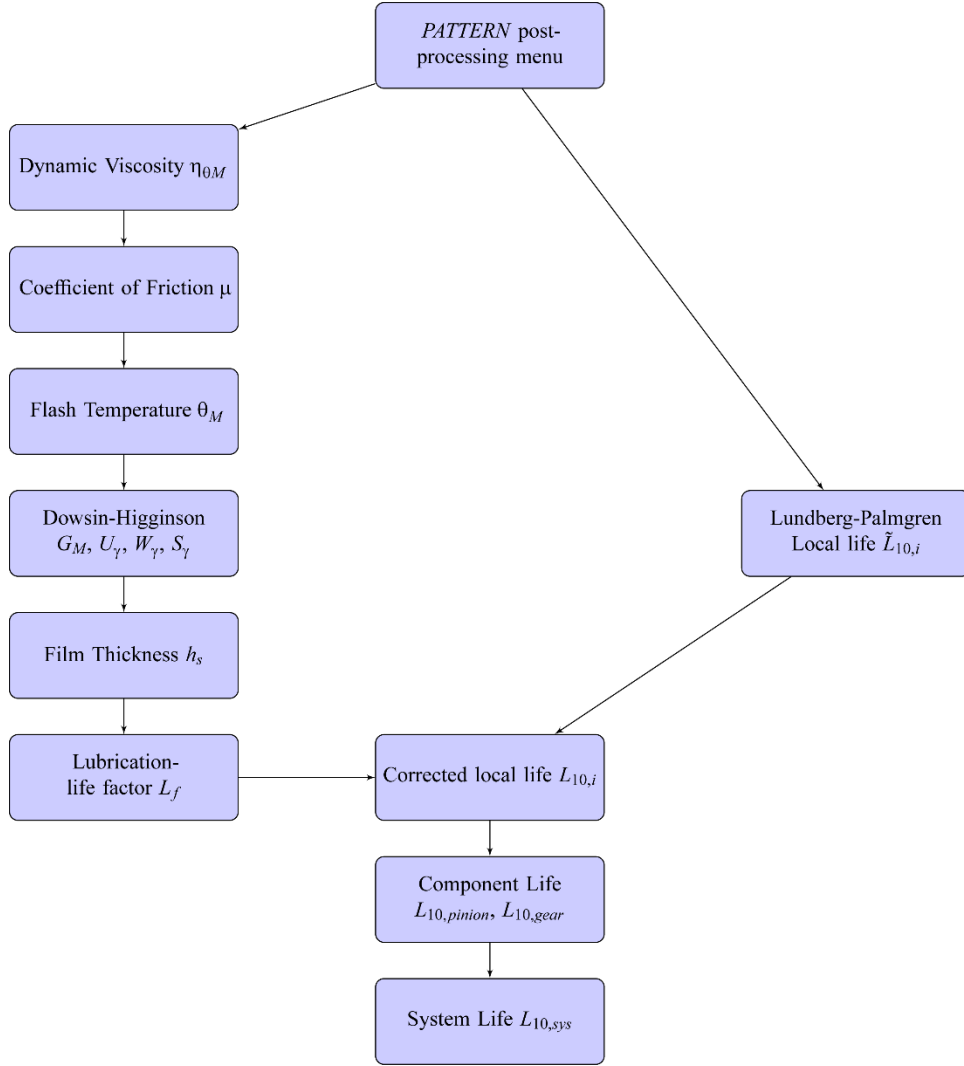


Figure 28.—The flow chart for surface durability calculations.

## 5.0 Bending Life

Bending fatigue occurs in the fillet region of the pinion and gear, and is distinct from the contact fatigue phenomenon observed in the contacting zone. Figure 29 and Figure 30 show snapshots of the variation of the maximum principal normal stress  $s_1$  over the pinion and gear surfaces. The peak tensile values occur on the concave side fillet of the pinion and the convex side fillet of the gear.

If we search for the maximum  $s_1$  in the profile direction, and over all time instances for individual face cross sections of individual teeth, it is possible to generate a graph of the type shown in Figure 31 for the pinion, and Figure 32 for the gear. In these graphs, each curve represents an individual tooth. Each data point on the curve represents the maximum over all time instances and profile positions.

If we follow the point on the pinion fillet that has the maximum value of  $s_1$ , then the time history of  $s_1$  for that point is shown in Figure 33. The time-history of a similar point on the gear is shown in Figure 34.

Similarly, the instantaneous distribution of minimum principal normal stress  $s_3$  on the pinion and gear is shown in Figure 35 and Figure 36. Graphs of minimum values over all profile locations and time values as a function of face location are shown in Figure 37 for the pinion, and Figure 38 for the gear. Figure 39 and Figure 40 show the variation of  $s_3$  with time, at the point with minimum  $s_3$ , on the pinion and gear respectively.

The peak values of  $s_1$  and  $s_3$  do not occur at the same place on the fillet. Hence the peak  $s_1$  and  $s_3$  cannot be used simultaneously for calculating the fatigue life. Instead the local values of  $s_1$  and  $s_3$  at every point on the fillet must be used to calculate a local life. The life of the gear or pinion will be the life at the point on the fillet with the shortest life.

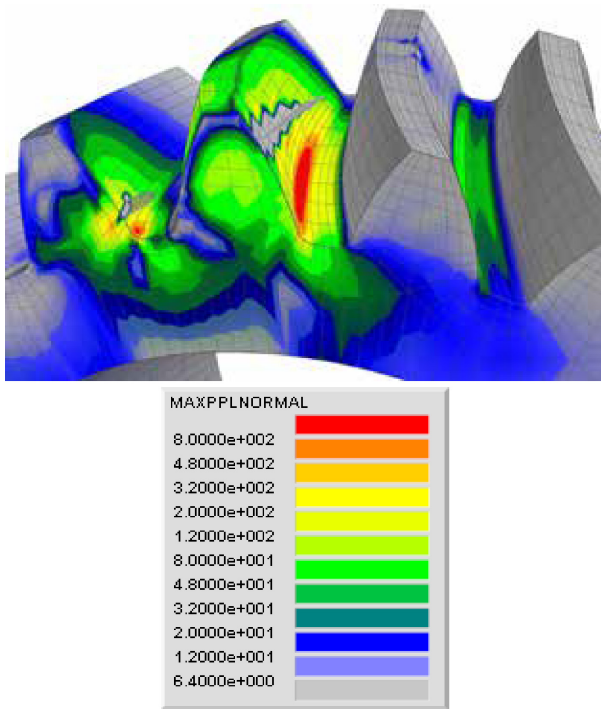


Figure 29.—Instantaneous maximum principal normal stress  $s_1$  variation over the pinion surface at 8000 in-lb of gear torque

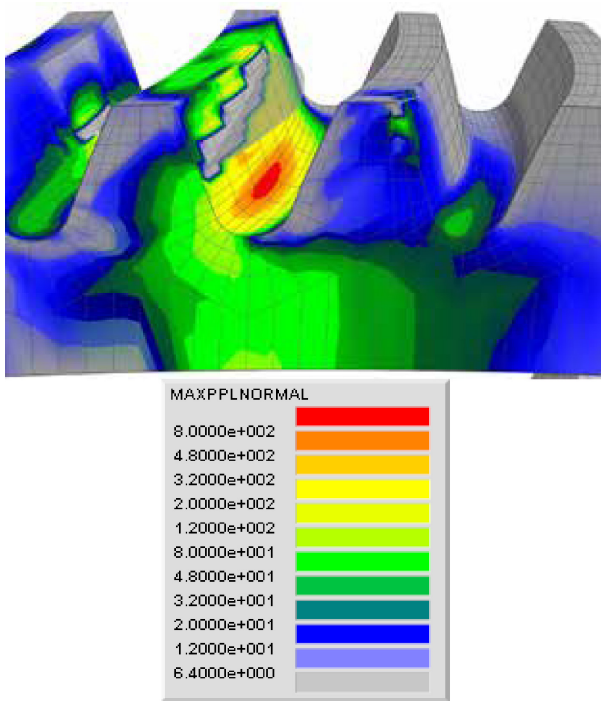


Figure 30.—Instantaneous maximum principal normal stress  $s_1$  variation over the gear surface at 8000 in-lb of gear torque

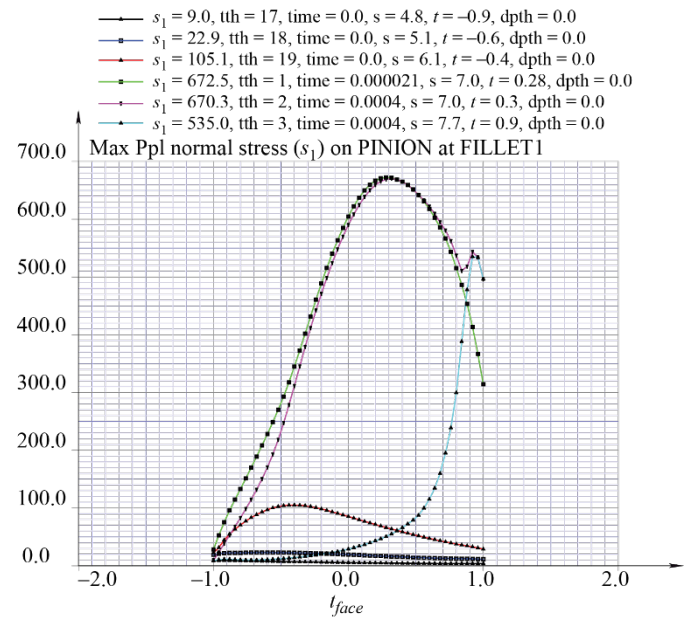


Figure 31.—Variation of the maximum of the maximum principal normal stress  $s_1$  over the face width of the pinion at 8000 in-lb of gear torque. Each curve represents an individual tooth. Each data point on the curve represents the maximum over all time instances and profile positions.  $t_{face} = -1.0$  is the toe end of the tooth and  $t_{face} = +1$  is the heel end. (Black=Tooth 17, Dark Blue=Tooth 18, Red=Tooth 19, Green=Tooth 1, Magenta=Tooth 2, Light Blue=Tooth 3).

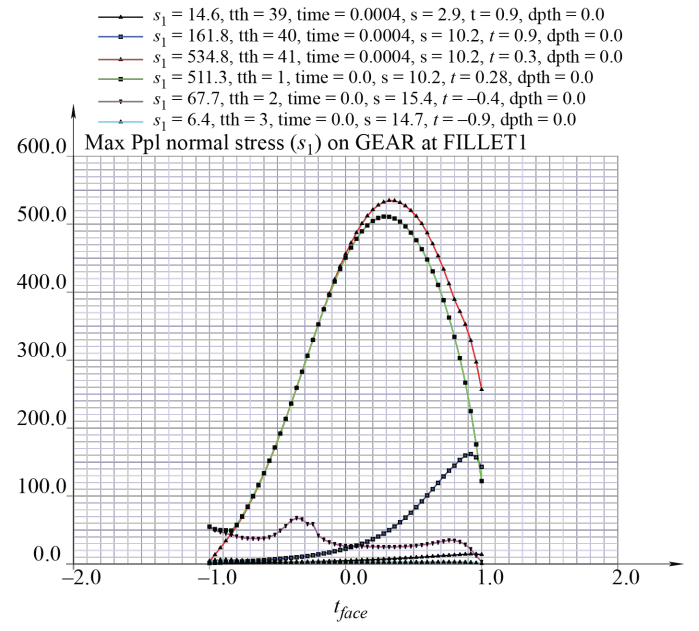


Figure 32.—Variation of the maximum of the maximum principal normal stress  $s_1$  over the face width of the gear at 8000 in-lb of gear torque. Each curve represents an individual tooth. Each data point on the curve represents the maximum over all time instances and profile positions.  $t_{face} = -1.0$  is the toe end of the tooth and  $t_{face} = +1$  is the heel end. (Black=Tooth 39, Dark Blue=Tooth 40, Red=Tooth 41, Green=Tooth 1, Magenta=Tooth 2, Light Blue=Tooth 3).

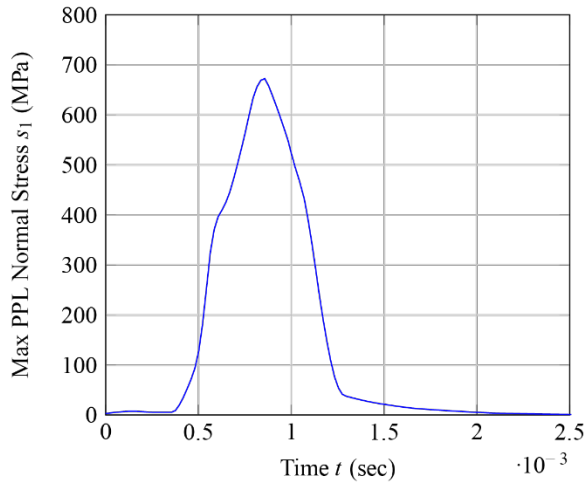


Figure 33.—Time history  $s_1(t)$  at the point on the pinion fillet that has the maximum value of  $s_1$ .

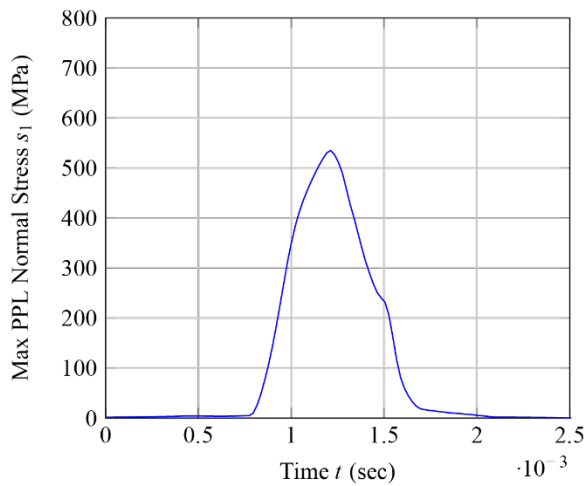


Figure 34.—Time history  $s_1(t)$  at the point on the gear fillet that has the maximum value of  $s_1$ .

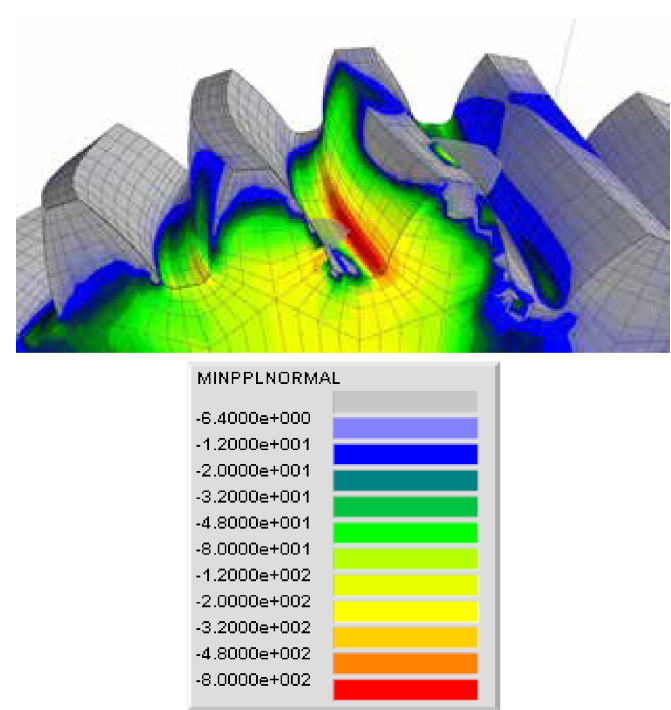


Figure 35.—Instantaneous minimum principal normal stress  $s_3$  variation over the pinion surface at 8000 in-lb of gear torque

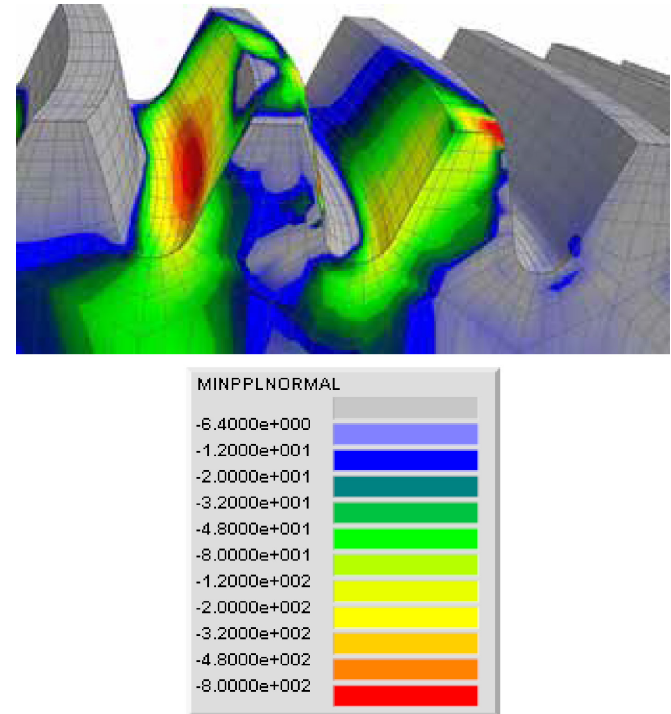


Figure 36.—Instantaneous minimum principal normal stress  $s_3$  variation over the gear surface at 8000 in-lb of gear torque

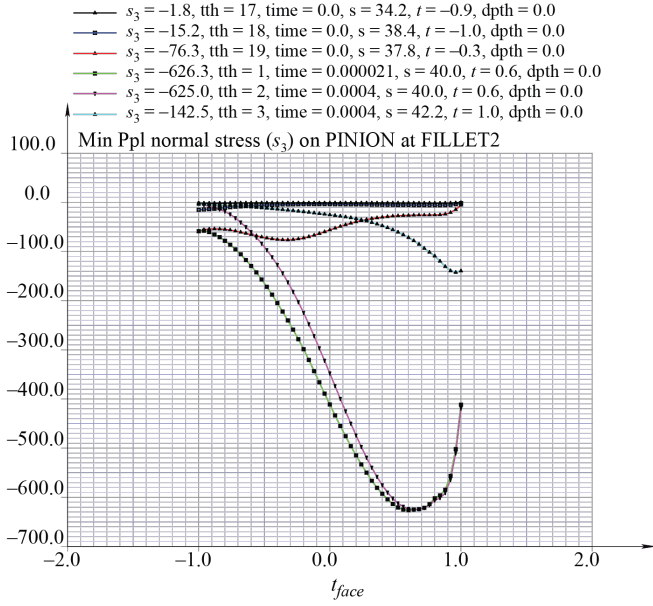


Figure 37.—Variation of the minimum of the minimum principal normal stress  $s_3$  over the face width of the pinion at 8000 in-lb of gear torque. Each curve represents an individual tooth. Each data point on the curve represents the minimum over all time instances and profile positions.  $t_{face} = -1.0$  is the toe end of the tooth and  $t_{face} = +1$  is the heel end. (Black=Tooth 17, Dark Blue=Tooth 18, Red=Tooth 19, Green=Tooth 1, Magenta=Tooth 2, Light Blue=Tooth 3).

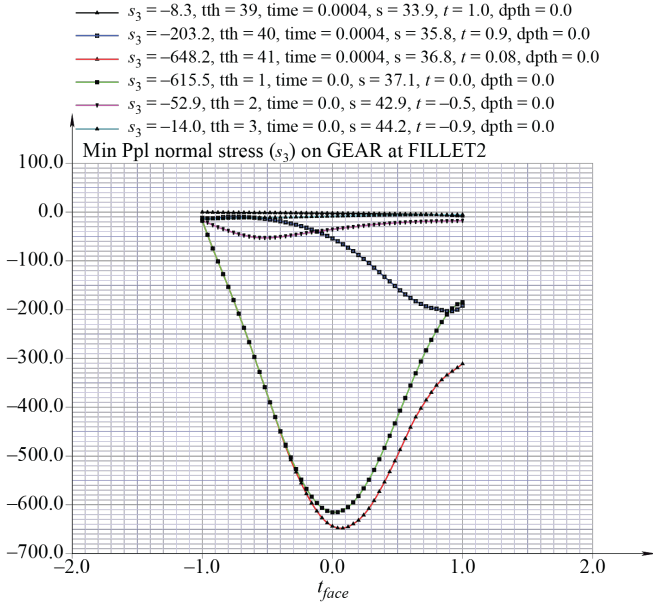


Figure 38.—Variation of the minimum of the minimum principal normal stress  $s_3$  over the face width of the gear at 8000 in-lb of gear torque. Each curve represents an individual tooth. Each data point on the curve represents the minimum over all time instances and profile positions.  $t_{face} = -1.0$  is the toe end of the tooth and  $t_{face} = +1$  is the heel end. (Black=Tooth 39, Dark Blue=Tooth 40, Red=Tooth 41, Green=Tooth 1, Magenta=Tooth 2, Light Blue=Tooth 3).

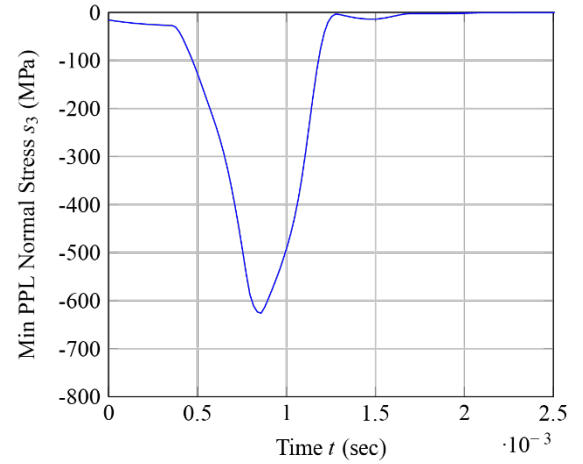


Figure 39.—Time history  $s_3(t)$  at the point on the pinion fillet that has the minimum value of  $s_3$ .

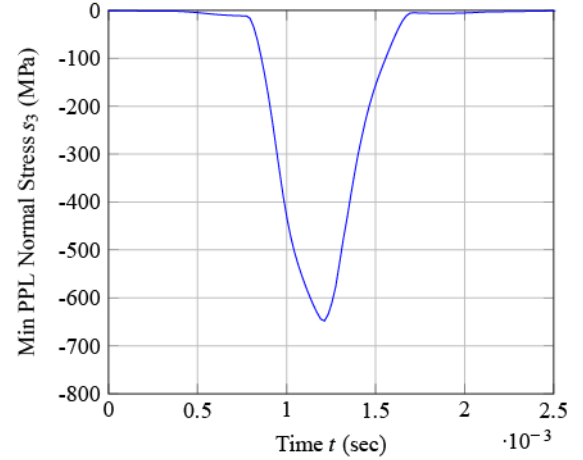


Figure 40.—Time history  $s_3(t)$  at the point on the gear fillet that has the minimum value of  $s_3$ .

To calculate local bending life at any point on the fillet, we look at the time-history of stress at that fillet point. Our model was run for exactly one mesh-cycle: each tooth has advanced by exactly one tooth pitch over the analysis time range. Since all teeth in our model are identical, we can replicate the entire stress history of a single tooth as it goes all the way around by splicing together predictions on all individual teeth. This allows us to compute the maximum (over time) of the maximum principal normal stress  $s_1$  and the minimum (over time) of the minimum principal normal stress  $s_3$  at each point on the fillet. Then we compute the local alternating stress  $s_{alt}$  and mean stress  $s_{mean}$  values:

$$s_{mean} = \frac{\max(s_1) + \min(s_3)}{2}$$

$$s_{alt} = \frac{\max(s_1) - \min(s_3)}{2}$$

A specimen under purely alternating uniaxial stress amplitude  $s_{eq}$  would be equivalent to the state of stress at this fillet point  $(s_{mean}, s_{alt})$  if

$$s_{eq} = \begin{cases} s_{alt} & \text{when } s_{mean} \leq 0 \\ \frac{s_{alt}}{1 - s_{mean} / S_{ult}} & \text{otherwise} \end{cases} \quad (9)$$

A Haigh diagram (Figure 41 for example) is an X-Y plot in which the X axis represents the mean stress  $s_{mean}$  and the Y axis represents the alternating stress  $s_{alt}$ . The values of  $(s_{mean}, s_{alt})$  at individual fillet points appear as discrete points on the Haigh diagram. For the points lying on the right of the vertical axis,  $s_{eq}$  is the intersection point of the vertical axis with a line through  $(s_{mean}, s_{alt})$  and  $(S_{ult}, 0)$ .  $S_{ult}$  is the ultimate tensile strength (see Table 7). For points that lie on the left of the vertical axis,  $s_{eq}$  is the same as  $s_{alt}$ .

Figure 41 shows Haigh diagram for the pinion concave side (tensile side) fillet, at 8000 in-lb of gear torque. There were 2500 fillet points processed, creating a cloud of 2500 points on the graph. Fillet points that were closer than 2.0 mm from the closest contact point were discarded, because the finite elements are too large to give usable numbers very close to the concentrated loading generated by the contact.

The two red lines indicate the points on the fillet that have the highest value of  $s_{eq}$ , and the highest value for  $s_{alt}$ . The point with the highest  $s_{eq}$  is considered the critical point for bending fatigue failure. Figure 42 shows a similar plot for the pinion convex side (compressive side) fillet.

TABLE 7.—STRENGTH PARAMETERS USED IN THE FATIGUE CALCULATION

Ultimate strength, $S_{ult}$ .....	1585 MPa
Yield strength, $S_{yield}$ .....	1515 MPa
Endurance limit, $S_{end}$ .....	700 MPa

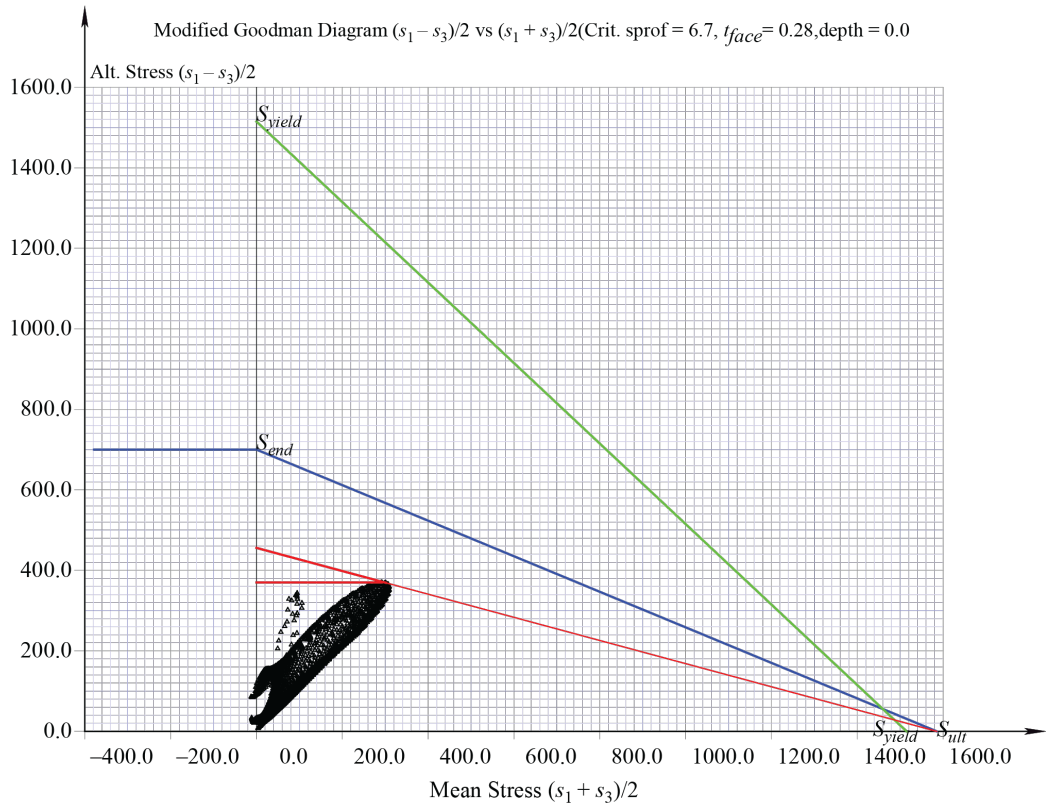


Figure 41.—Haigh diagram for the tensile (concave) side fillet of the pinion at 8000 in-lb of gear torque.

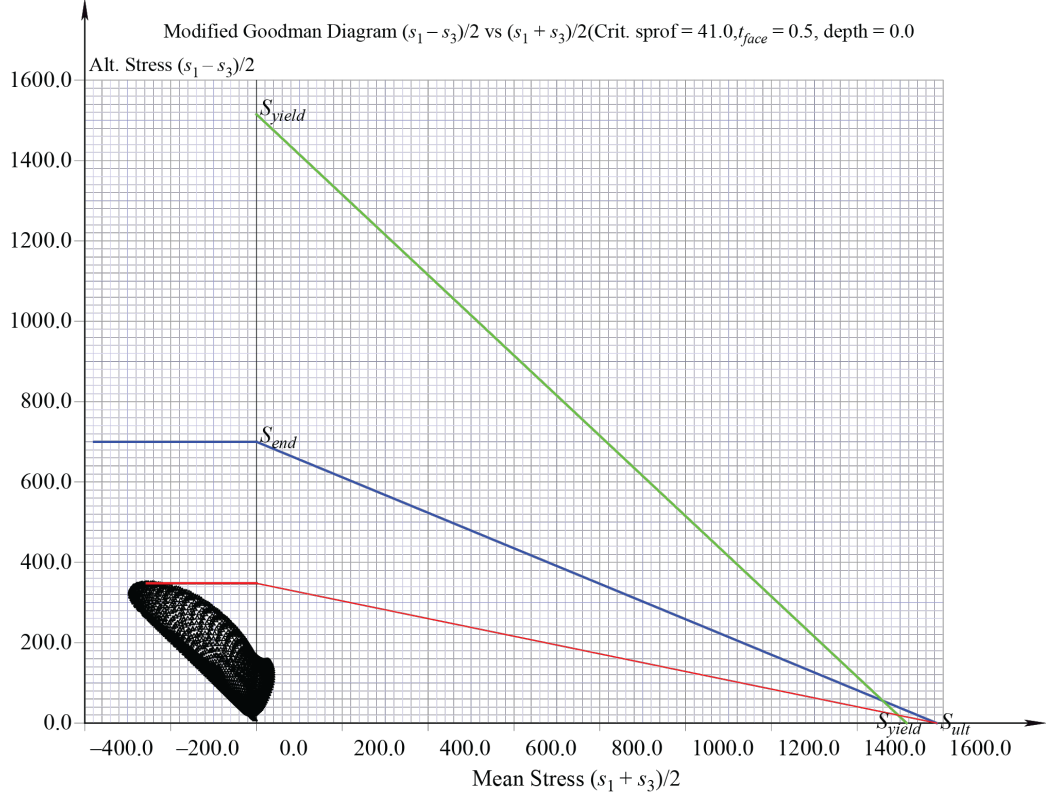


Figure 42.—Haigh diagram for the compressive (convex) side fillet of the pinion at 8000 in-lb of gear torque.

The blue line which connects  $(S_{ult}, 0)$  to  $(0, S_{end})$  demarcates the boundary between points with infinite life, and points with finite life. Any point  $(s_{mean}, s_{alt})$  that lies above the blue line would generate a value for  $s_{eq}$  higher than the endurance limit  $S_{end}$ , and would fail under fatigue after a finite number of cycles. Any point that lies below the blue line would have infinite life.

The green line on the Haigh diagram joins  $(S_{yield}, 0)$  with  $(0, S_{yield})$ , and demarcates the separation between points that undergo tensile yielding ( $\max_t(s_1) > S_{yield}$ ) in the first load cycle, and those that will not.  $S_{yield}$  is the tensile yield strength.

Figure 43 and Figure 44 show similar plots for the tensile and compressive side fillets of the gear, at 8000 in-lb of gear torque. All data points in these four Haigh diagrams lie below the blue fatigue line, which indicates that the pinion and gear will not fail from bending fatigue.

In order to demonstrate the fatigue failure calculation method, another analysis was also run at 12,000 in-lb and 16,000 in-lb of gear torque.

The Haigh diagrams for 12,000 in-lb of gear torque are shown in Figure 45 to Figure 48. At 12,000 in-lbf of gear torque, both compressive side fillets exhibit infinite life. The pinion tensile side fillet is well above the finite life boundary, while the gear tensile side fillet is marginal, just barely below the boundary.

The Haigh diagrams for 16,000 in-lb of gear torque are shown in Figure 49 to Figure 52. At 16,000 in-lb of gear torque, only the gear compressive side fillet (Figure 53) shows infinite life. The data points for the other 3 Haigh diagrams show points that have  $s_{eq}$  larger than the endurance limit.

We shall discuss the pinion tensile side fillet in more detail. The entire time history of  $s_1(t)$  and  $s_3(t)$  at the point on the pinion tensile side fillet that has the maximum equivalent pure alternating stress  $s_{eq}$  is shown in Figure 54 for 12,000 in-lbf of gear torque and Figure 55 for 16,000 in-lbf of gear torque. The strains  $\varepsilon_1(t)$  and  $\varepsilon_3(t)$  at the same points are shown in Figure 56 for 12,000 in-lbf of gear torque and Figure 57 for 16,000 in-lbf of gear torque. The samples between  $t = 0.007$  sec and  $t = 0.00725$  sec have been discarded from these plots because the fillet point was too close to the contact zone during that time interval. The *FATIGUE* post-processing menu writes out a large amount of information for all the fillet points in tab delimited form. This tab-delimited data is ready to be processed by any convenient computer program. We used Excel to load the data into a spreadsheet and make two dimensional contour plots. Figure 58 and Figure 59 are two such plots showing the variation of mean stress  $s_{mean}$  and alternating stress  $s_{alt}$  over the fillet at 12000 in-lb of gear torque. The equivalent pure alternating stress  $s_{eq}$  is also calculated using Equation (9) and output to the tab-delimited file. Its variation over the fillet surface is shown in Figure 60.

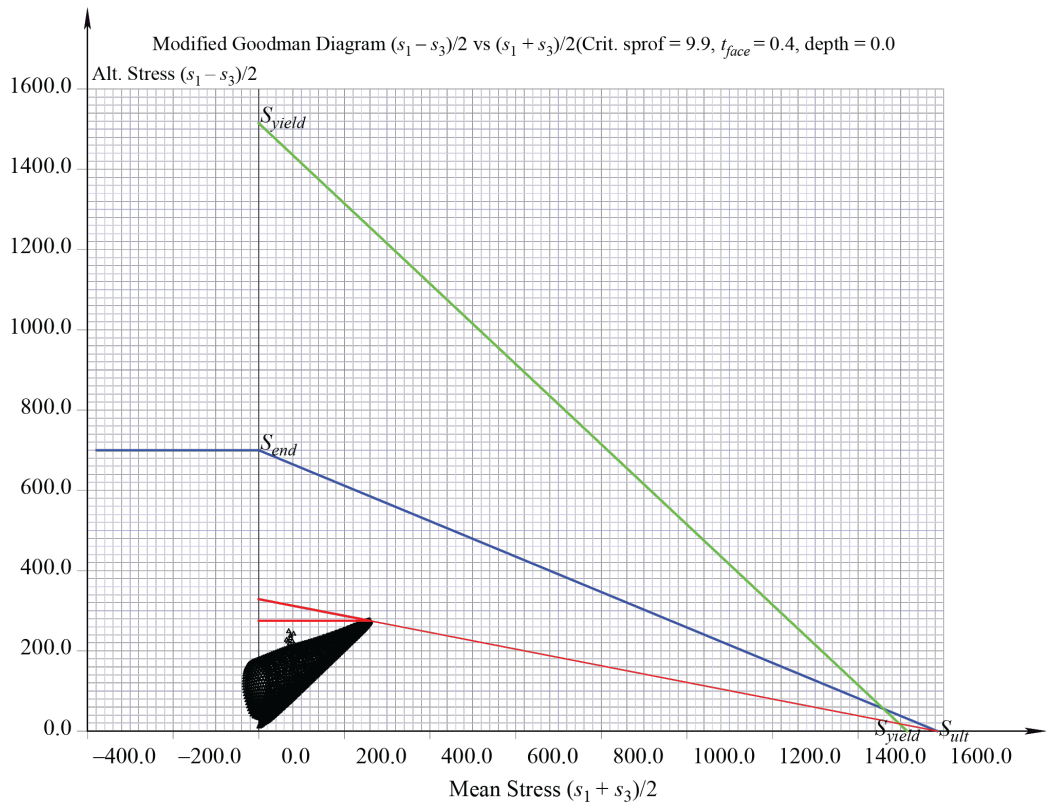


Figure 43.—Haigh diagram for the tensile (convex) side fillet of the gear at 16000 in-lb of gear torque.

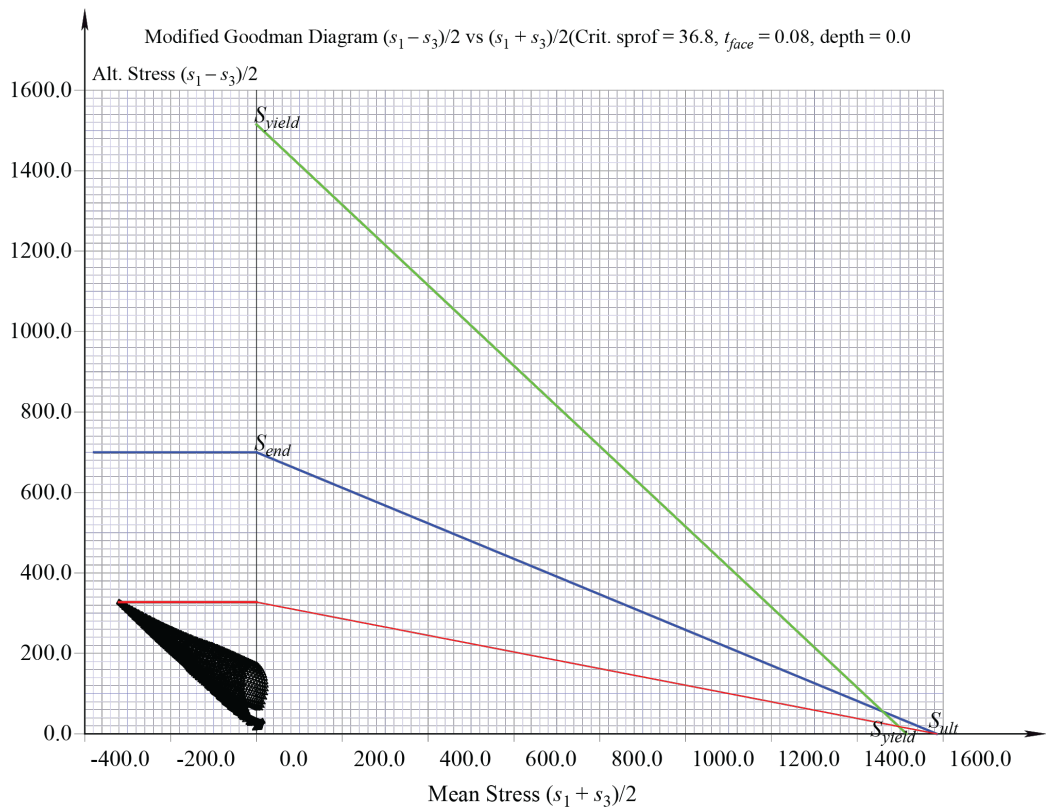


Figure 44.—Haigh diagram for the compressive (concave) side fillet of the gear at 8000 in-lb of gear torque.

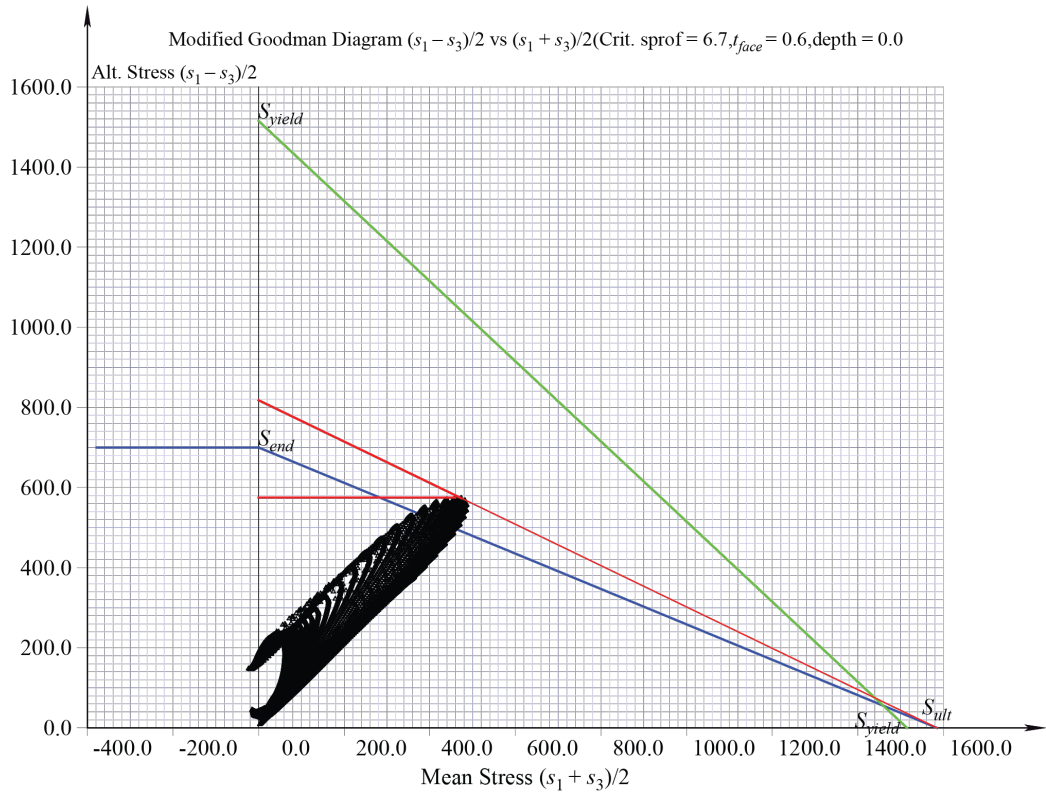


Figure 45.—Haigh diagram for the tensile (concave) side fillet of the pinion at 12000 in-lb of gear torque.

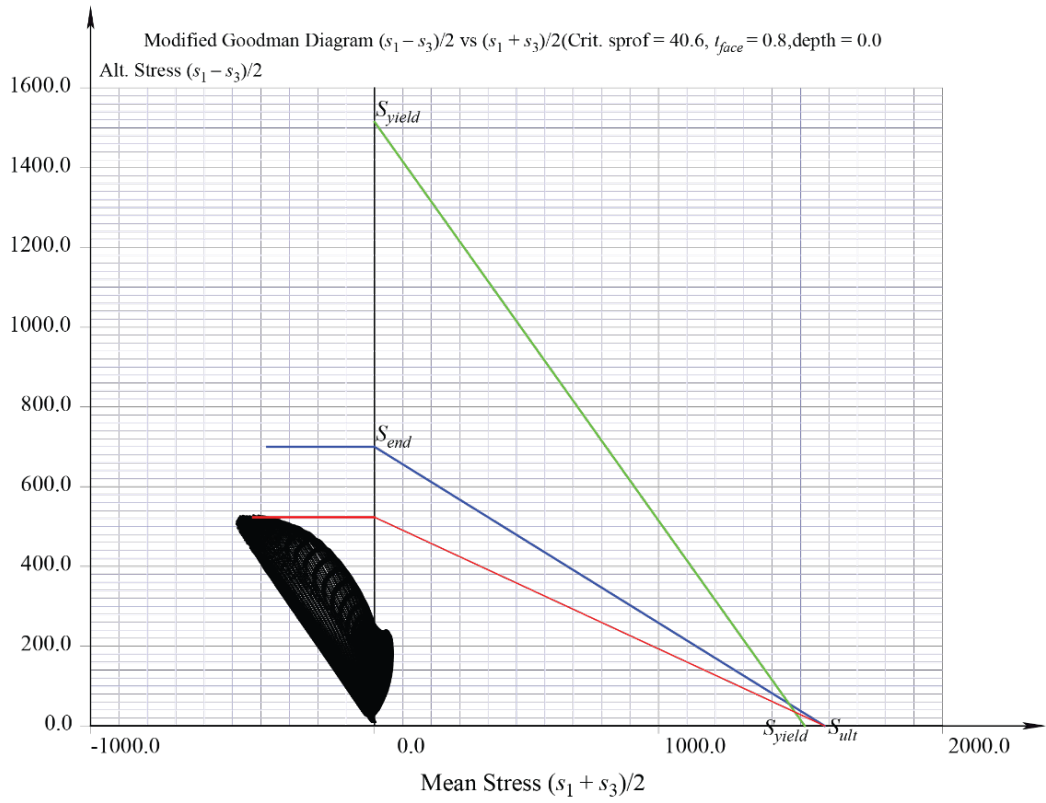


Figure 46.—Haigh diagram for the compressive (convex) side fillet of the pinion at 12000 in-lb of gear torque.

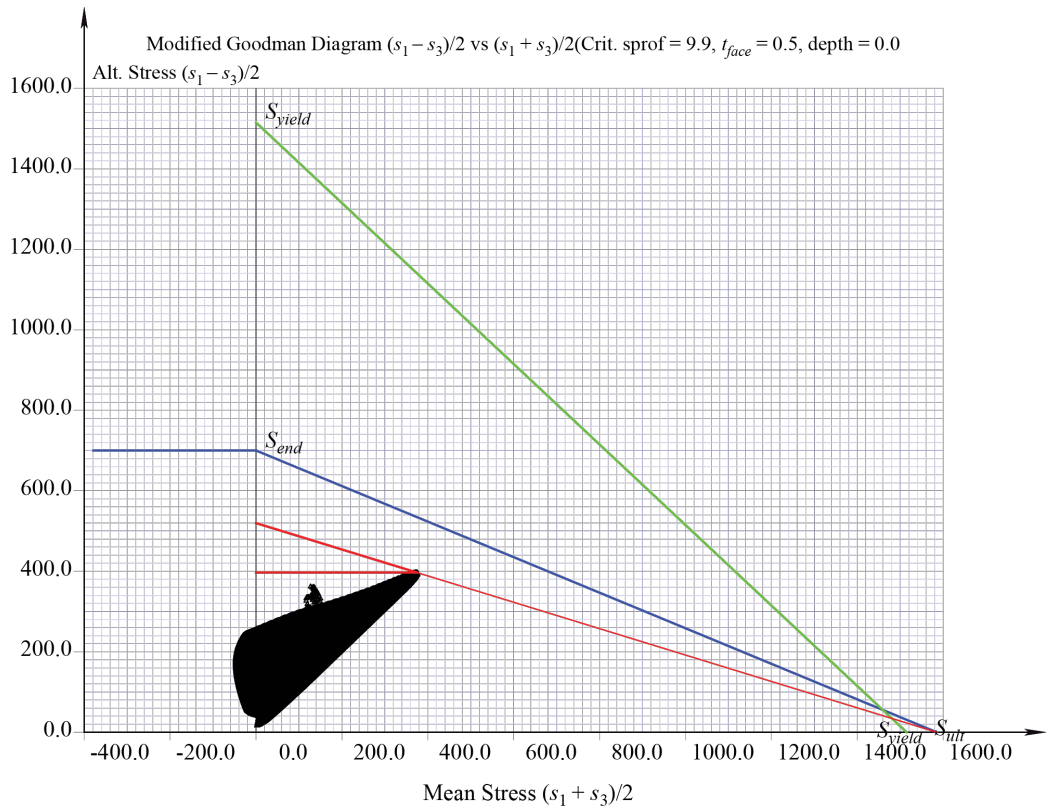


Figure 47.—Haigh diagram for the tensile (convex) side fillet of the gear at 12000 in-lb of gear torque.

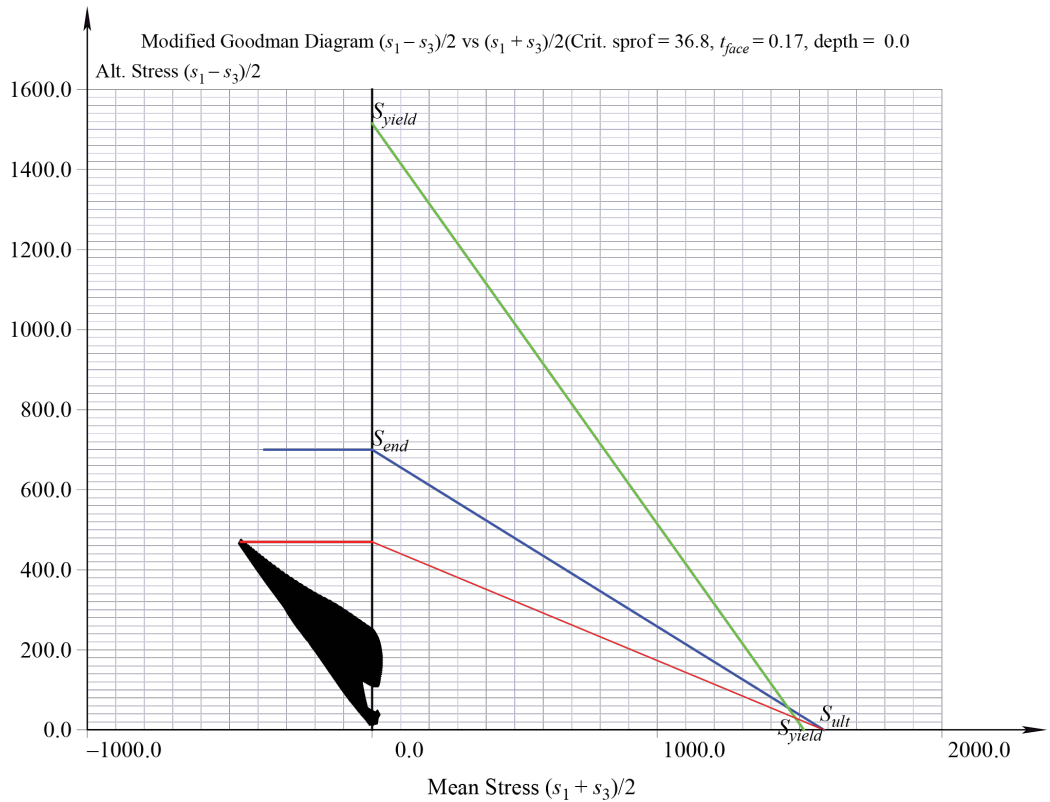


Figure 48.—Haigh diagram for the compressive (concave) side fillet of the gear at 12000 in-lb of gear torque.

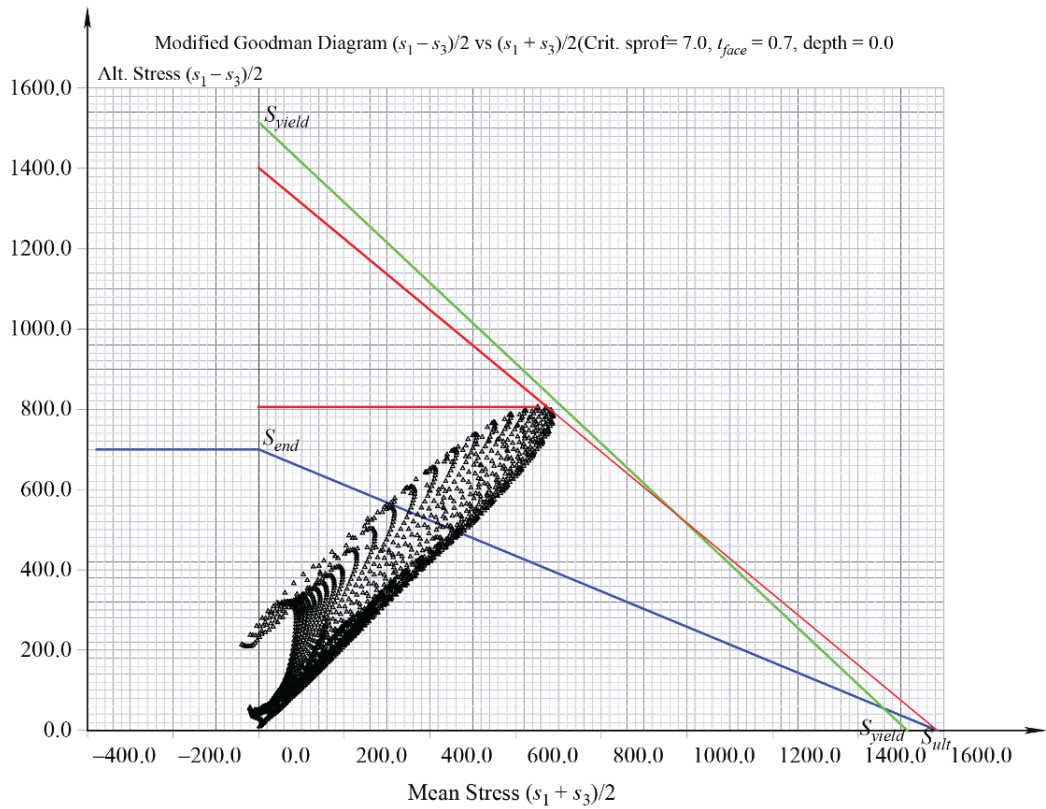


Figure 49.—Haigh diagram for the tensile (concave) side fillet of the pinion at 16000 in-lb of gear torque.

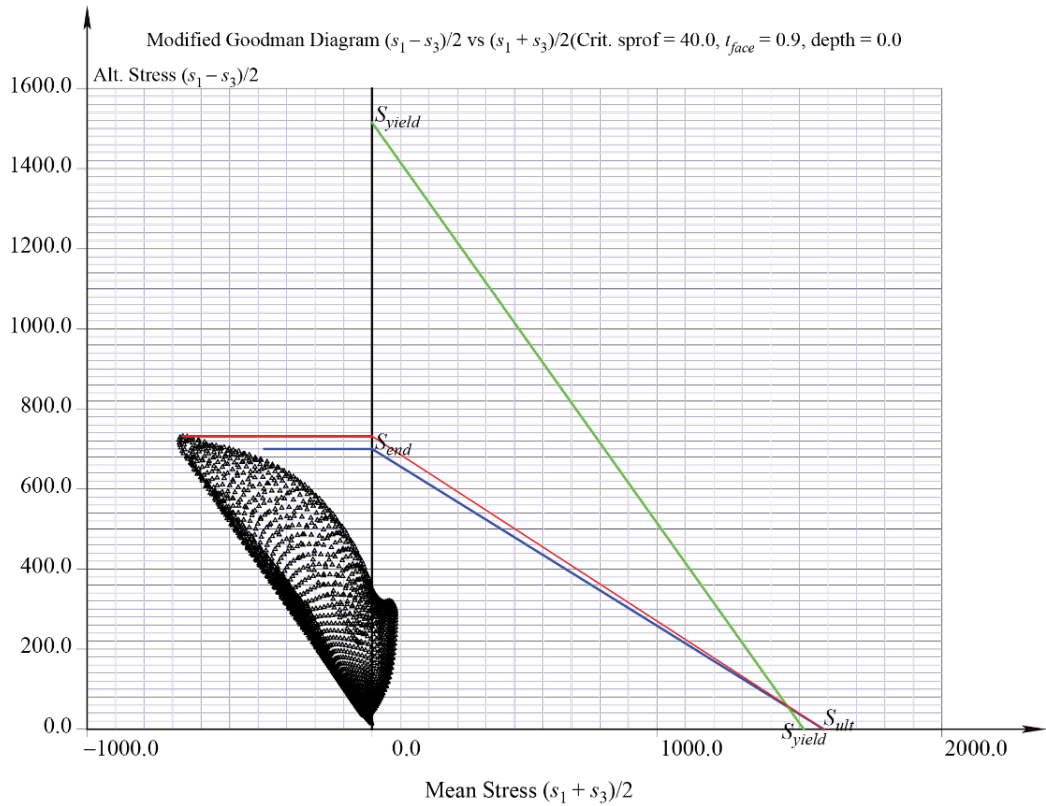


Figure 50.—Haigh diagram for the compressive (convex) side fillet of the pinion at 16000 in-lb of gear torque.

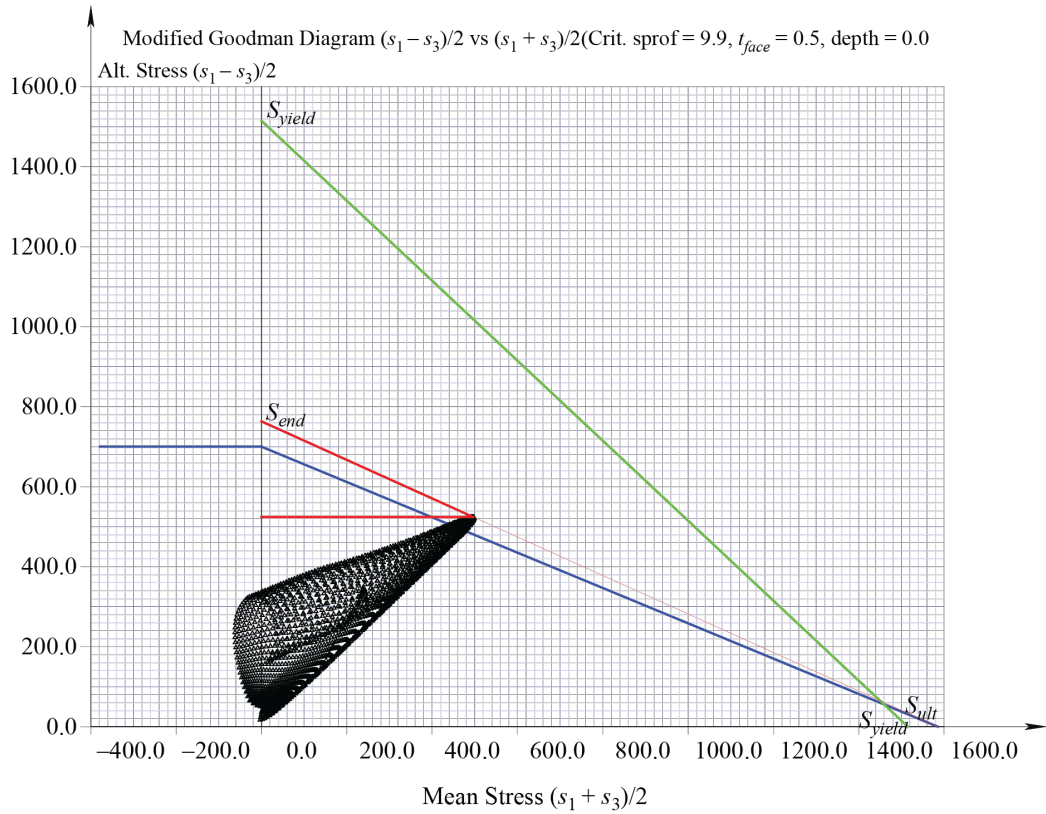


Figure 51.—Haigh diagram for the tensile (convex) side fillet of the gear at 16000 in-lb of gear torque.

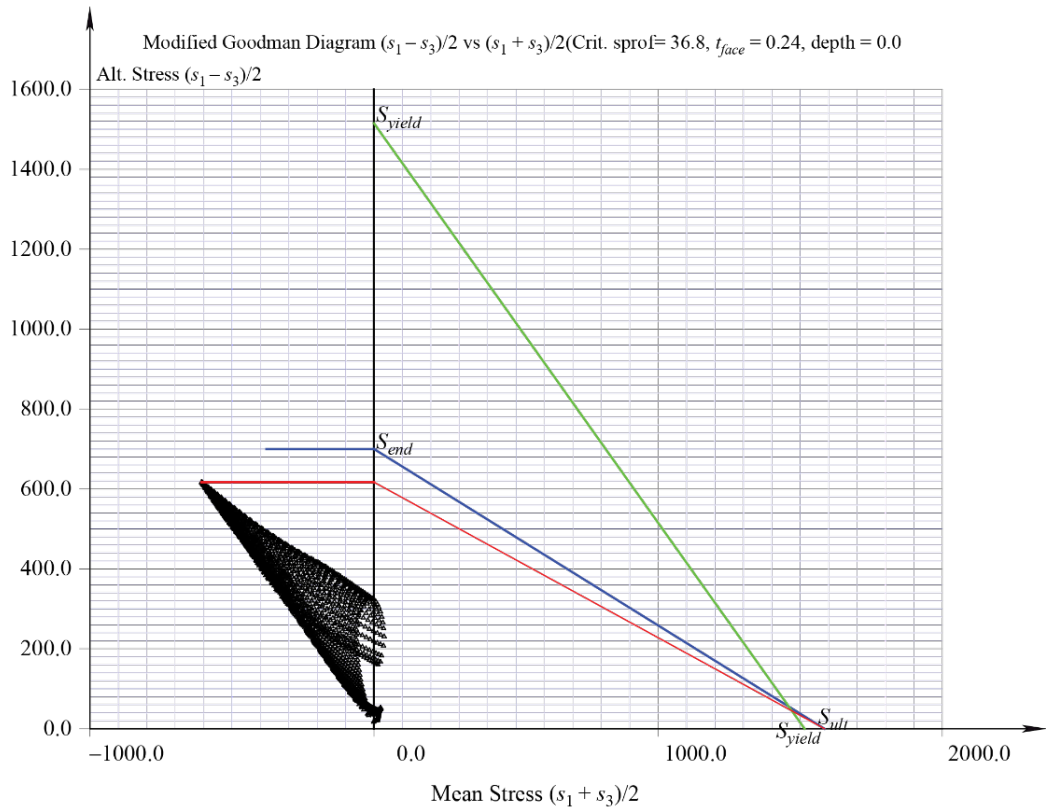


Figure 52.—Haigh diagram for the compressive (concave) side fillet of the gear at 16000 in-lb of gear torque.

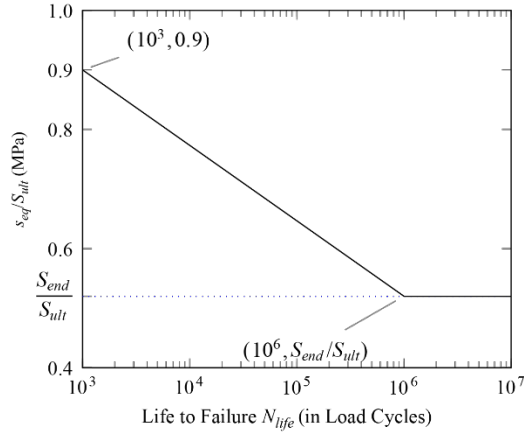


Figure 53.—An S-N curve commonly used for steel (Ref. 14).

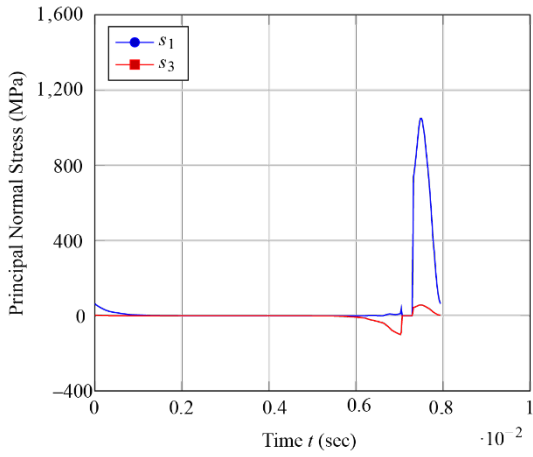


Figure 54.—Time history of maximum principal normal stress  $s_1(t)$  and  $s_3(t)$  at the point on the pinion tensile side fillet that has the maximum value of  $s_{eq}$ . The gear torque was 12,000 in-lb.

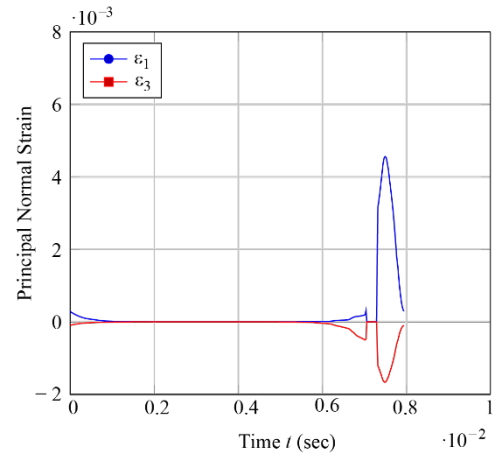


Figure 56.—Time history of maximum principal normal strain  $\varepsilon_1(t)$  and  $\varepsilon_3(t)$  at the point on the pinion tensile side fillet that has the maximum value of  $s_{eq}$ . The gear torque was 12,000 in-lb.

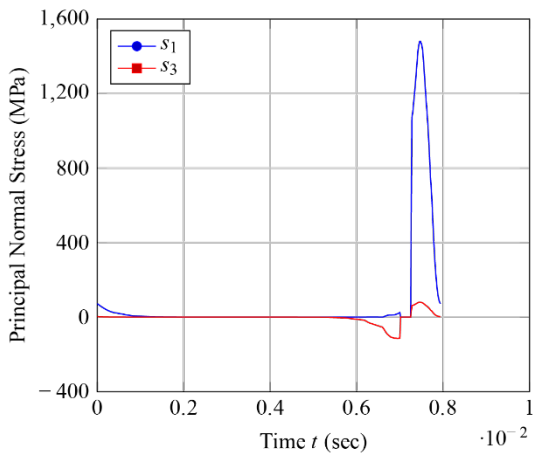


Figure 55.—Time history of maximum principal normal stress  $s_1(t)$  and  $s_3(t)$  at the point on the pinion tensile side fillet that has the maximum value of  $s_{eq}$ . The gear torque was 16,000 in-lb.

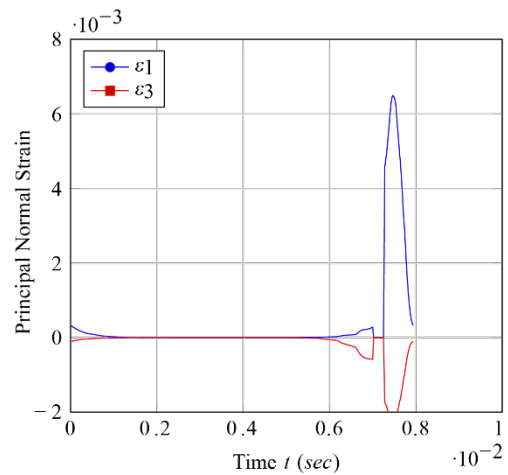


Figure 57.—Time history of maximum principal normal strain  $\varepsilon_1(t)$  and  $\varepsilon_3(t)$  at the point on the pinion tensile side fillet that has the maximum value of  $s_{eq}$ . The gear torque was 16,000 in-lb.

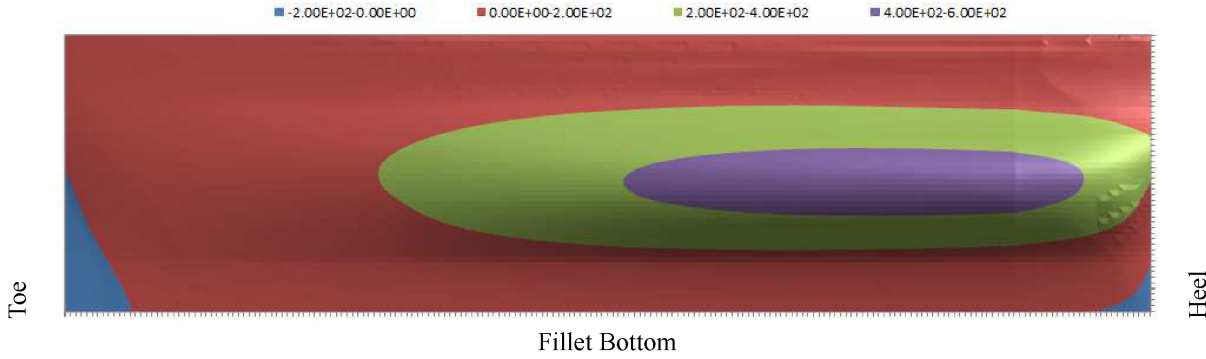


Figure 58.—Map of mean stress  $s_{mean}$  (MPa) drawn on the tensile side pinion fillet, at 12,000 in-lb of gear torque.

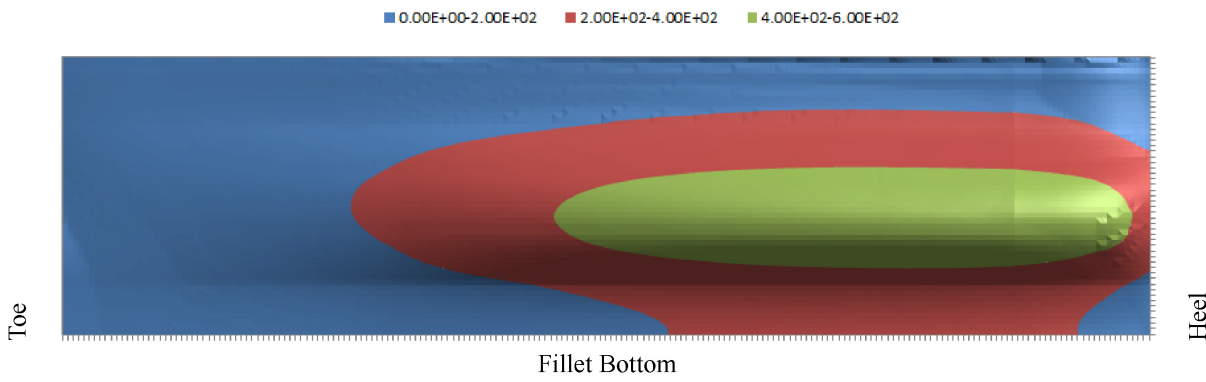


Figure 59.—Map of alternating stress  $s_{alt}$  (MPa) drawn on the tensile side pinion fillet, at 12,000 in-lb of gear torque.

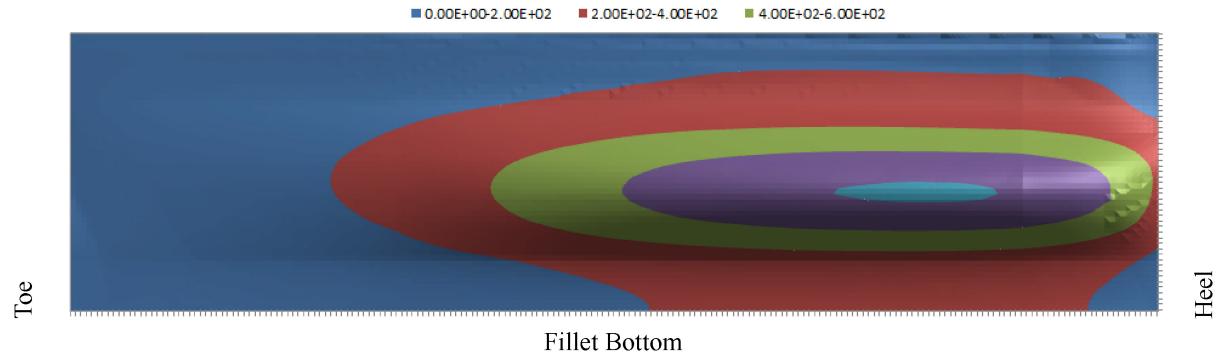


Figure 60.—Map of equivalent pure alternating  $s_{eq}$  (MPa) drawn on the tensile side pinion fillet, at 12,000 in-lb of gear torque.

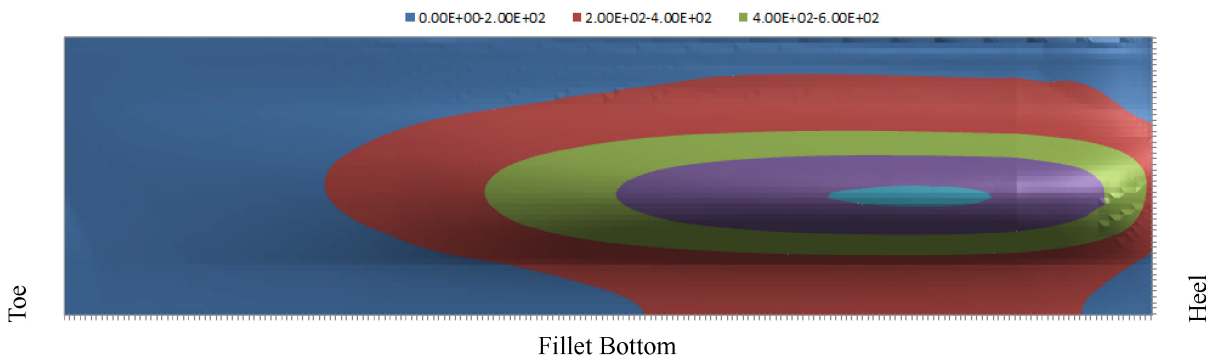


Figure 61.—Map of damage  $D$  over 1,000 load cycles drawn on the tensile side pinion fillet, at 12,000 in-lb of gear torque.

Similar maps for 16,000 in-lb of gear torque are shown in Figure 62 to Figure 64.

The local life  $N_{life}$  is related to the local  $s_{eq}$  through an  $S - N$  curve. Various forms of  $S - N$  curve are available, and should be chosen based on the application. For demonstration purposes we use a very simple  $S - N$  curve commonly used for steel, based on a text-book stress-life failure theory (Ref. 14). This theory assumes that the life of steel is infinite when  $s_{eq} < S_{end}$ , life at  $s_{eq} = S_{end}$  is  $N_{life} = 10^6$  load cycles, that the life at  $s_{eq} = S_{1000} \cong 0.9S_{ult}$  is  $N_{life} = 10^3$  load cycles, and that in between these two points, the  $S - N$  curve is a straight line when the life axis is in log scale, as shown in Figure 53.

This  $S - N$  curve can be represented by

$$N_{life} = \begin{cases} \infty & \text{when } s_{eq} < S_{end} \\ 10^{-C/b} s_{eq}^{1/b} & \text{when } s_{eq} > S_{end} \end{cases} \quad (10)$$

or

$$s_{eq} = 10^c N_{life}^b \text{ when } 10^3 < N_{life} < 10^6 \quad (11)$$

where the constants  $b$  and  $C$  are calculated to generate a straight line on the graph:

$$b = -\frac{1}{3} \log_{10} \frac{S_{1000}}{S_{end}}$$

$$C = \log_{10} \frac{(S_{1000})^2}{S_{end}}$$

At 12,000 in-lb of gear torque, the point on the pinion tensile fillet with minimum life had  $N_{life} = 222,016$  load cycles. At 16,000 in-lb of gear torque, this dropped down to  $N_{life} = 1,190$  load cycles.

The local damage fraction  $D$  at each point on the fillet after  $N$  load cycles is defined as the fraction:

$$D = N / N_{life}$$

where  $N_{life}$  is the predicted local life at that fillet point. Figure 61 shows a map of damage distribution over the fillet after  $N = 1,000$  load cycles at 12,000 in-lb of gear torque and Figure 65 shows a map of damage distribution over the fillet after  $N = 1,000$  load cycles at 16,000 in-lb of gear torque. The region with  $D > 1.0$  is predicted to fail according to this simple stress-life theory.

These damage distribution maps are easily used to compute cumulative damage when the pinion is subjected to varying load conditions. We would simply run a separate analysis for each loading condition  $i$ , and obtain damage distribution plots for  $D_i$  using the process described above. Then, using Miner's rule, we simply add the damage distributions to get the cumulative damage distribution:

$$D = \sum_i D_i \quad (13)$$

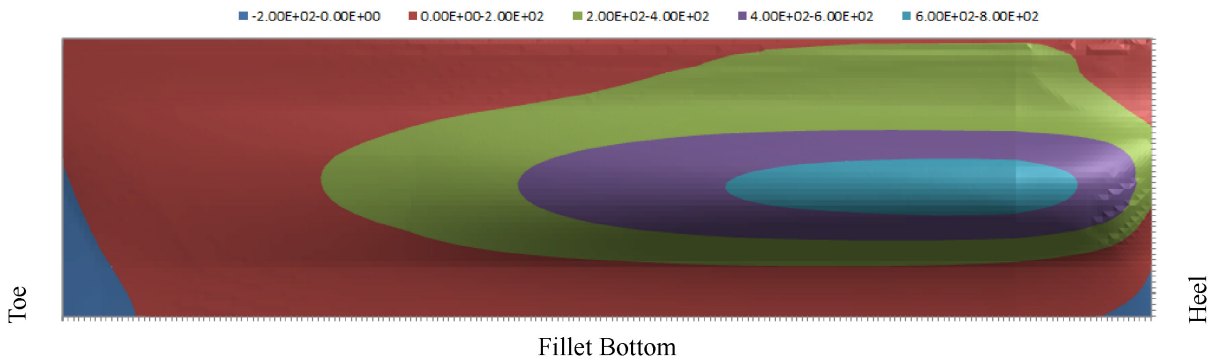


Figure 62.—Map of mean stress  $s_{mean}$  (MPa) drawn on the tensile side pinion fillet, at 16,000 in-lb of gear torque.

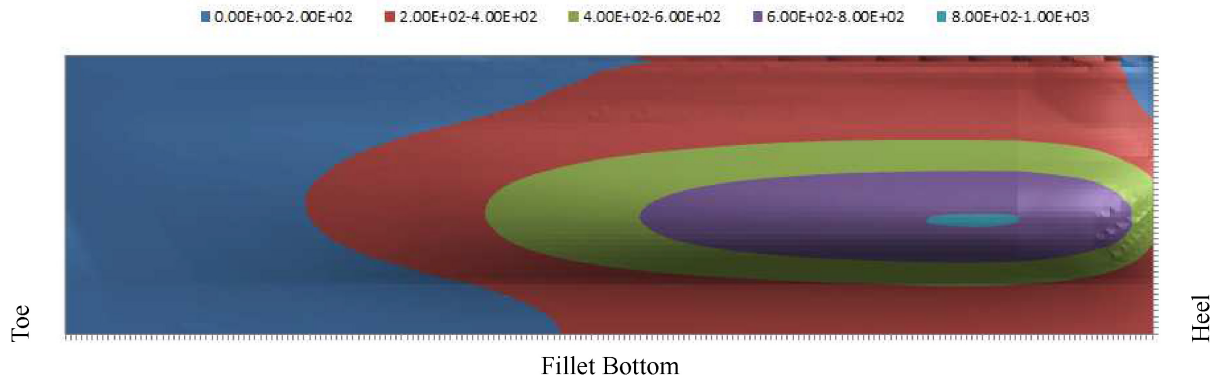


Figure 63.—Map of alternating stress  $s_{alt}$  (MPa) drawn on the tensile side pinion fillet, at 16,000 in-lb of gear torque.

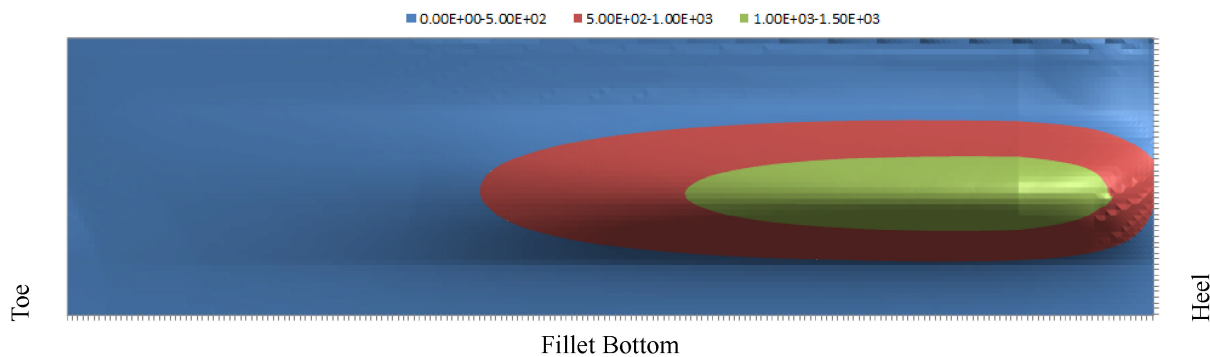


Figure 64.—Map of equivalent pure alternating  $s_{eq}$  (MPa) drawn on the tensile side pinion fillet, at 16,000 in-lb of gear torque.

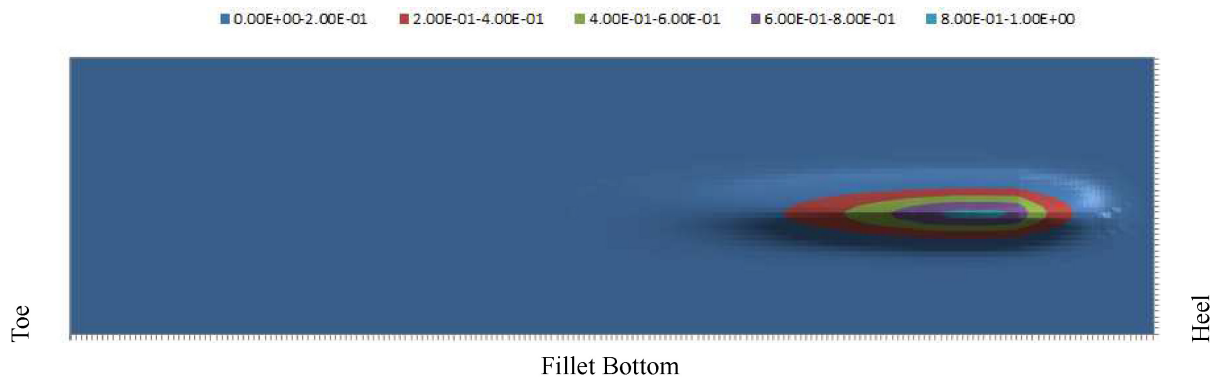


Figure 65.—Map of damage  $D$  over 1,000 load cycles drawn on the tensile side pinion fillet, at 16,000 in-lb of gear torque.

## 6.0 Results and Conclusion

Surface and bending durability calculations were implemented and demonstrated. The surface durability calculation was compared with test data. The test data agrees with the surface durability life calculations about as well as can be expected from a limited sample size. We did not attempt to fit the Weibull parameters to the test data because we would need more test evidence to override published results. The calculations presented here are included in the Transmission3D, HypoidFaceMilled and HypoidFaceHobbed packages, and in Excel macros which will be provided to NASA along with the necessary license keys.

## References

1. J. C. Skurka. Elastohydrodynamic lubrication of roller bearings. *Journal of Lubrication Technology, Transactions of the ASME*, (ASME Paper Number 69-LUB-18), 1969.
2. ISO. Calculation of micropitting load capacity of cylindrical spur and helical gears - part 1: Introduction and basic principles. Standard ISO/TR 15144-1:2010(E), International Organization for Standardization, Geneva, Switzerland, 2010.
3. Timothy M. Krantz and Ahmet Kahraman. An experimental investigation into the influence of the lubricant viscosity and additives on gear wear. Technical Report NASA/TM—2005-213956, NASA, Lewis Research Center, 2005.
4. D. Dowson and G. R. Higginson. *Elastohydrodynamic Lubrication*. Pergamon Press, Oxford, 1966.
5. S. M. Poplawski, J. V. Peters and E. V. Zaretsky. Effect of roller profile on cylindrical roller bearing life prediction—part i: Comparison of bearing life theories. *Tribol. Trans., STLE*, 44(3):339–350, 2001.
6. S. M. Poplawski, J. V. Peters and E. V. Zaretsky. Effect of roller profile on cylindrical roller bearing life prediction—part ii: Comparison of roller profiles. *Tribol. Trans., STLE*, 44(3):417–427, 2001.
7. Steven M. Poplawski, Joseph V. Peters and Ervin V. Zaretsky. Effect of roller profile on cylindrical roller bearing life prediction. Technical Report NASA/TM—2000-210368, NASA, Glenn Research Center, 2000.
8. Ervin V. Zaretsky. Roller bearing life prediction, theory and application. Technical Report NASA/TM—2013-215305, NASA, Glenn Research Center, 2013.
9. W. J. Anderson. Elastohydrodynamic lubrication theory as a design parameter for rolling element bearings. *ASME design engineering conference and show*, (ASME Paper Number 70-DE-19), 1970.
10. Ervin V. Zaretsky. A. Palmgren revisited - a basis for bearing life prediction. Technical Memorandum 107440, NASA Glenn Research Center, 1997.
11. Bogdan Warda and Agieszka Chudzik. Fatigue life prediction of the radial roller bearing with the correction of roller generators. *International Journal of Mechanical Sciences*, 89:299–310, 2014.
12. Dennis P. Coy, John J. Townsend and Ervin V. Zaretsky. Analysis of dynamic capacity of low-contact-ratio spur gears using Lundberg-Palmgren theory. Technical Note NASA TN D-8029, NASA, Lewis Research Center, 1975.
13. W. Weibull. A statistical theory of the strength of materials. *Ingenjörers Vetenskaps Akademien (Proceedings of the Royal Swedish Academy of Engineering)*, (151), 1939.
14. Jess J. Bannantine, Julie A. Comer and James L. Handrock. *Fundamentals of Metal Fatigue Analysis*. Prentice-Hall, Inc., Upper Saddle River, New Jersey, 1990.



